Geothermics 132 (2025) 103453

Contents lists available at ScienceDirect

Geothermics

journal homepage: www.elsevier.com/locate/geothermics

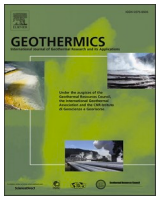

Reservoir quality controls in the Lower Buntsandstein and their relation to detrital grain size, URG, SW-Germany

Benjamin Busch [a,*], Lennart L. Böke [a,1], Christina Schmidt [b], Matthias Warnecke [b], Christoph Hilgers [a]

[a] Structural Geology and Tectonics, Institute of Applied Geosciences, Karlsruhe Institute of Technology, Adenauerring 20a, 76131 Karlsruhe, Germany
[b] Vulcan Energie Ressourcen GmbH, Amalienbadstraße 41, Bau 54, 76227 Karlsruhe, Germany

ARTICLE INFO

Keywords:
Chemical compaction
Pressure dissolution
Diagenesis
Reservoir quality
Upper Rhine Graben
Buntsandstein

ABSTRACT

Reservoir quality of the Lower Triassic Buntsandstein in the Upper Rhine Graben (URG) is currently being explored to better assess the possibility of geothermal production and associated lithium brine production. Previous studies highlight a generally positive effect of increased detrital grain size and blocky cement content on elevated porosity and permeability, while outlining a generally negative influence of compactional processes, which are enhanced by tangential illite grain coatings and to a lesser extent by ductile rock fragments.

This overall assessment can be supported by the studied samples from a research well (Kraichgau-1002) on the western graben shoulder, penetrating the coarser-grained Lower Buntsandstein at present-day depths between 500 and 710 m. The overall porosity and permeability is low (2.9 to 16.0 %, <0.0001 to 7.8 mD) in the studied core section. Tangential illite grain coatings enhance the effect of chemical compaction, whereas blocky cements (quartz, K-feldspar, carbonates, anhydrite) stabilize the grain framework against mechanical compaction.

In samples with the same porosity in this study, higher permeability is found in samples with a coarser grain size. However, when also including other available Buntsandstein core samples, the overall correlation between permeability and grain size is poor (R^2=0.05). Furthermore, a reported correlation between clay mineral grain coating characteristics (grain-to-IGV and grain-to-grain coating coverage) and detrital grain size could not be established (R^2<0.01 and R^2=0.19, respectively) for neither the studied samples, nor the combined Buntsandstein sample series from core material. Therefore, the detrital grain size by itself is an unsuitable criterion to assess Buntsandstein reservoir quality in the marginal basin facies.

However, the extension of available datasets, which assess reservoir quality controls in the Buntsandstein in the area surrounding the URG highlights, that the previously defined reservoir quality controls are affecting larger areas of the marginal facies of the Buntsandstein present in NE France and SW Germany.

1. Introduction

Reservoir quality is one of the key elements of any successful utilization of the subsurface during the energy transition and decarbonization (Underhill et al., 2023), especially in areas showing abnormally high geothermal gradients like the Upper Rhine Graben (URG) (Clauser and Villinger, 1990). While the clear focus in terms of a geothermal utilization of the Triassic Buntsandstein in the URG is on the exploitation of natural fracture networks (Haffen et al., 2013; Bertrand et al., 2018), the sandstone matrix pore space may be an additional storage volume in light of by-production of e.g., lithium from geothermal brines (Slunitschek et al., 2021), to access the largest possible fluid volume. Previous studies on Buntsandstein core material from the graben center (Busch et al., 2022a), 1100–1500 m present day depth highlight a compactional dominated porosity loss. Economic porosity and permeabilities (porosity >15 %, permeability >100 mD) were preserved in medium-grained sandstone samples containing quartz and dolomite cements (Busch et al., 2022a). Illite cementation and chemical compaction along illite-coated quartz grain contacts, predominantly in finer-grained sandstones, were deteriorating reservoir quality (Busch et al., 2022a). This overall trend was also observed in more deeply buried Buntsandstein samples from the graben center (Busch et al.,

* Corresponding author.
E-mail address: benjamin.busch@kit.edu (B. Busch).
[1] Present address: REMEX SüdWest GmbH, Werftstraße 12, 76189 Karlsruhe, Germany.

https://doi.org/10.1016/j.geothermics.2025.103453
Received 18 April 2025; Received in revised form 4 July 2025; Accepted 17 July 2025
Available online 23 July 2025

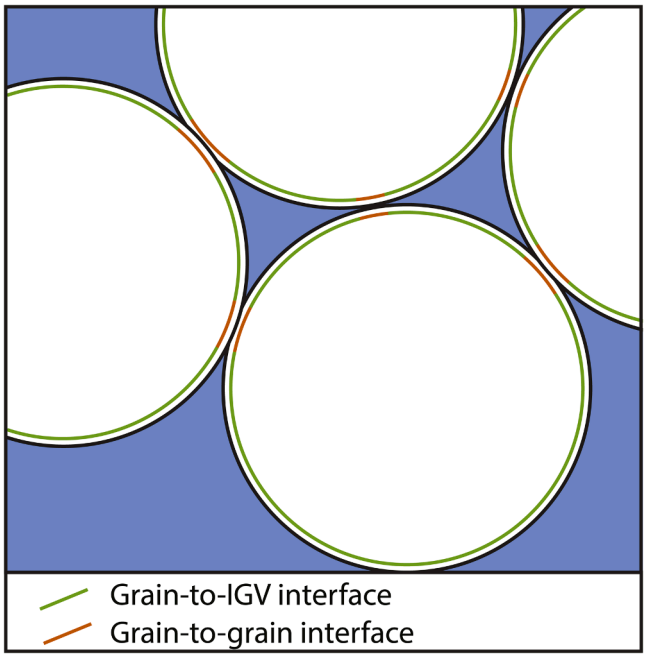

Fig. 1. Sketch of grain to IGV interfaces (orange) and grain to grain interfaces (GTG) in sands and sandstones (modified after Busch et al. (2024)).

2024), ~3000 m TVD present day depth and outcrop-based studies (Schmidt et al., 2020a; Schmidt, 2022), as well as from shallow exploration wells from the eastern graben shoulder (Quandt et al., 2022). However, the effectiveness of these processes has been shown to be closely related to the burial history. Samples subjected to higher thermal exposure (temperature over time) show more extensive quartz cementation, while uncemented samples exhibit lower intergranular volumes (IGV) due to enhanced chemical compaction (i.e., pressure dissolution) at illite coated grain contacts (Busch et al., 2024). However, the Römerberg oilfield near Speyer in the center of the URG is a testament to high reservoir quality preservation in Buntsandstein sandstones in fractured and porous reservoir sections (Böcker, 2020). Further studies relate the differences in reservoir quality in the Buntsandstein sandstones in the URG and surrounding areas to be controlled by quartz cement contents around faults and fractures (Bossennec et al., 2021), the detrital grain size (Busch et al., 2022a; Busch et al., 2024; Quandt et al., 2022; Schmidt et al., 2020a; Busch et al., 2022b; Bofill et al., 2025), or show a correlation to lithofacies (Bofill et al., 2025).

With multiple studies showing a general positive correlation between reservoir quality and detrital grain size (Busch et al., 2022a; Busch et al., 2024; Quandt et al., 2022; Schmidt et al., 2020; Busch et al., 2022b; Bofill et al., 2025), the detrital grain size may be a suitable criterion to locate high reservoir quality intervals. Larger detrital grain sizes in sandstones generally relate to higher permeability, as a function of larger pore throat sizes as compared to finer grain sizes and resulting narrower pore throats (e.g., Füchtbauer, 1998). As specifically the Lower Buntsandstein in the marginal basin facies follows a general coarsening upward trend and contains pebble-bearing sandstones (e.g.,

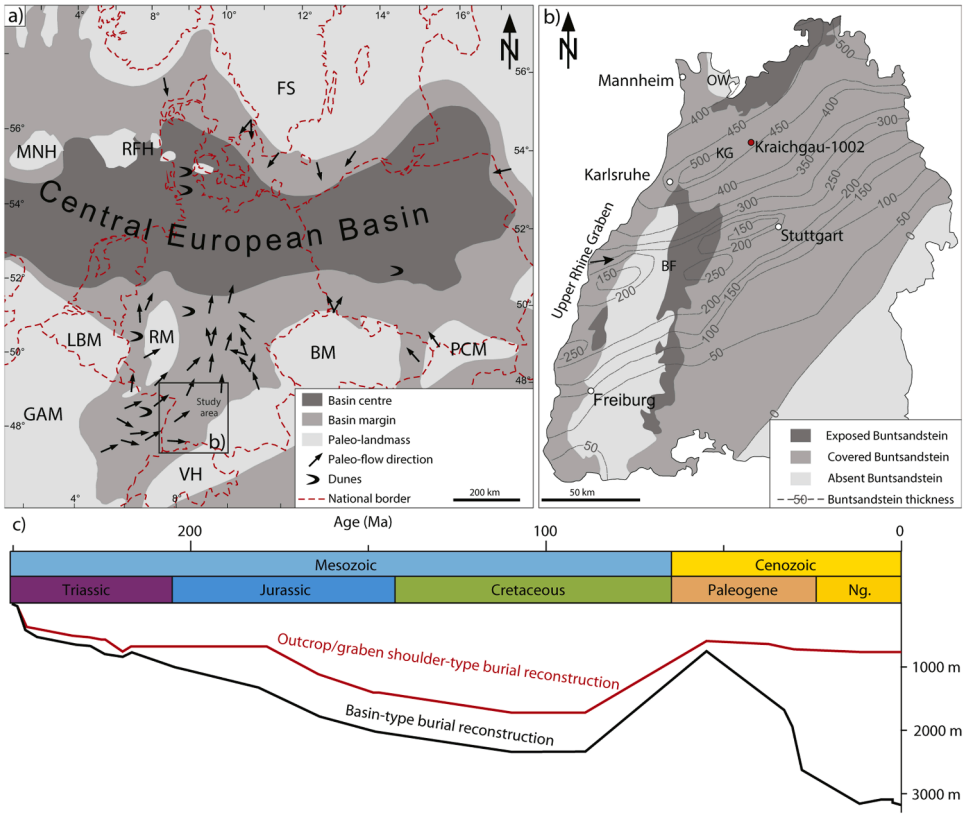

Fig. 2. a) Paleogeographic overview of the Central European Basin (Germanic Basin) with the reconstructed paleo-transport directions during the Lower Triassic (modified after Röhling and Lepper (2013) and Quandt et al. (2022). b) Map of the State of Baden-Württemberg in SW-Germany showing the location of the studied well and the reconstructed Buntsandstein thickness (modified after Rupf and Nitsch (2008), Leiber and Bock (2014), and Quandt et al. (2022)). c) Schematic burial history of the Buntsandstein for an outcrop type and basin type in the present day Upper Rhine Graben (modified after Bossennec et al. (2021), the outcrop type has been adjusted to match present day depths of the Buntsandstein in the studied well). BF: Black Forest, BM: Bohemian Massif, FS: Fennoscandian Shield, GAM: Gallic-Armorican Massif, KG: Kraichgau, LBM: London-Brabant Massif, MNH: Mid-North Sea High, OW: Odenwald, PCM: Proto-Carpathian Massif, RFH: Ringkøbing-Fyn High, RM: Rhenish Massif, VM: Vindelician Massif.

Leiber and Bock, 2014), the Lower Buntsandstein may be a suitable target to explore and exploit geothermal resources if this correlation can be extended across available, published core samples.

Furthermore, the detrital grain size has been correlated to grain coating characteristics (Aro et al., 2023; Shammari et al., 2011; Wooldridge et al., 2017). Generally, the presence of tangential illite grain coatings at grain-to-IGV (GTI) interfaces (orange in Fig. 1) has been linked to syntaxial quartz cement inhibition and preservation of porosity and permeability (Heald and Larese, 1974; Bloch et al., 2002), even at depth of e.g., 4800 m in Permian Rotliegendes eolian sandstones from the Southern Permian Basin in northern Germany (Monsees et al., 2020). However, the samples from the Rotliegendes also indicated enhanced chemical compaction in areas where grain-to-grain (GTG) interfaces (green in Fig. 1) are covered by tangential illite (Monsees et al., 2020). Similar observations have also been made for the fluvio-eolian sandstones of the Triassic Buntsandstein deposited in a semi-arid continental setting in the marginal facies of the Germanic Basin (Busch et al., 2024). Depending on the specific location on individual grain surfaces, tangential illite can therefore both preserve and deteriorate reservoir quality during burial. The effect of illite (or muscovite) to enhance intragranular pressure dissolution (chemical compaction) has been studied in sandstones for decades (Heald, 1955; Bjørkum, 1996; Stephenson et al., 1992; Oelkers et al., 1996; Wilson and Stanton, 1994), but has only been assigned to electrochemical surface potential differences at these mineral interfaces within the past 15 years (Greene et al., 2009; Kristiansen et al., 2011). Assessing sediment compaction can be seen as a standard approach in reservoir-geology, based on the widespread applications of concepts as the IGV (Paxton et al., 2002; Houseknecht, 1987) or compactional and cementational porosity loss calculations (COPL and CEPL, Lundegard, 1992). The degree of mechanical and chemical compaction is a function of the (vertical) effective stresses during sediment burial, the detrital grain composition (brittle vs. ductile grains), experienced temperatures, pore-pressure, pressure dissolution at grain contacts, and the onset of intergranular cementation/dissolution (Paxton et al., 2002).

Radial illitic grain coatings on the other hand have also been shown to successfully inhibit syntaxial quartz overgrowth cementation (Busch et al., 2022a) in the Triassic Buntsandstein and Permian Rotliegendes sandstones from the Netherlands (Busch et al., 2020; Molenaar and Felder, 2018; Gaupp and Okkerman, 2011). However, they have long been known to negatively affect permeability by narrowing hydraulic pore throat radii, especially if a pore-bridging texture is developed (Neasham, 1977). The formation of authigenic clay mineral coatings in buried sections of the Triassic Buntsandstein is related to hydrothermal activity within the URG and neighboring areas prior to the Tertiary (Clauer et al., 2008). Overall, the thermal evolution of reservoir sandstones will also have an influence on reservoir properties, as (i) detrital grain rheologies are affected by temperature (Evans and Kohlstedt, 1995) and (ii) syntaxial quartz precipitation kinetics have been shown to be temperature sensitive (Rimstidt and Barnes, 1980; Lander et al., 2008). Therefore, the assessment of the influence of diagenesis is key to an understanding of the controlling factors to predict economical or uneconomical reservoir quality in the Buntsandstein in the URG.

The main aim of this study is to assess the reservoir quality controls in the Lower Buntsandstein from a research well in the Kraichgau region (well Kraichgau-1002), east of the Upper Rhine Graben and assess the relation of diagenetic and detrital reservoir quality controls. Based on petrographic and petrophysical analyses, we will assess if the previously defined reservoir quality controls (grain size, quartz cement content and IGV as a function of grain coating clay minerals) are also applicable to the studied well, and if a relation between detrital grain sizes and grain coating characteristics can be established for samples from the studied well section and other available core samples from the Buntsandstein. Furthermore, we assess if petrophysical properties cluster distinctly as a function of petrographic properties (detrital and authigenic components, grain size) in the studied samples. Correlation with published samples from core material of the region may enable a more accurate targeting of high reservoir quality intervals in the Buntsandstein.

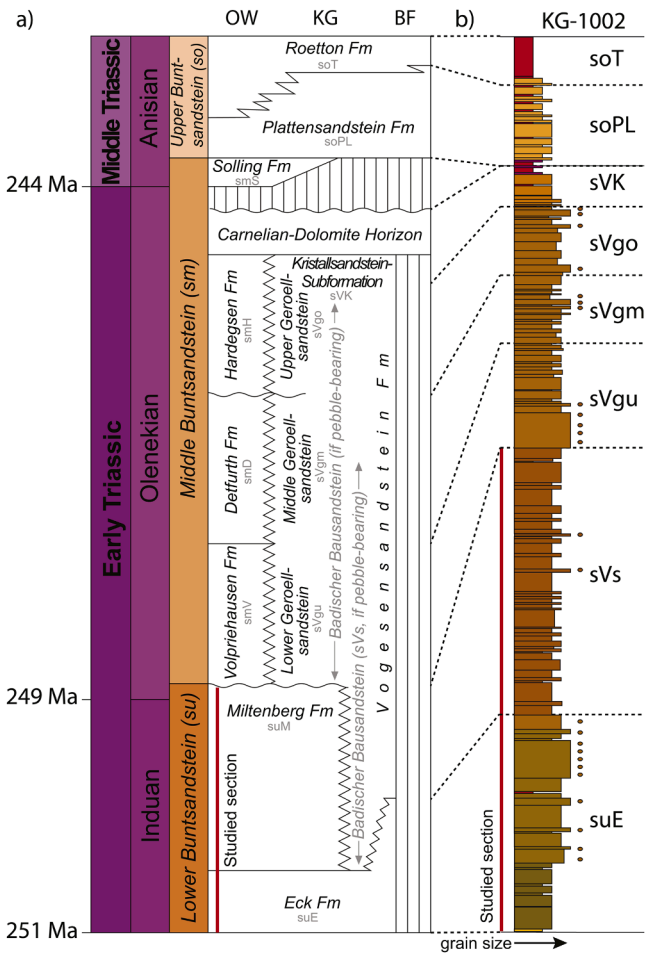

Fig. 3. a) Lithostratigraphic subdivision of the Triassic Buntsandstein with the studied section highlighted in red (modified after Geyer and Gwinner (2011), Leiber and Bock (2014), and Quandt et al. (2022)). b) Simplified lithological column of the studied core material (modified after Nitsch (2024)). Circles indicate gravelly horizons. OW: Odenwald, KG: Kraichgau, BF: Black Forest (For location see Fig. 2).

2. Geological setting

During the Lower Triassic, the margins of the Central European Basin (also Germanic Basin, Fig. 2a) accumulated continental deposits in a semi-arid to arid climate following the gradual Permian regression trend in central Europe (Füchtbauer, 1967; Ziegler, 1982; Aigner and Bachmann, 1992; Bourquin et al., 2011). Those conditions prevailed during the deposition of the fluvio-eolian sequence of the Buntsandstein, the lowermost part of the tripartite subdivision of the Germanic Triassic, overlain by the Muschelkalk and Keuper (Quandt et al., 2022).

The sediments of the marginal facies are sourced mainly from the Gallic-Armorican Massif to the west to west-southwest of the studied marginal basin facies in southern Germany (Bourquin et al., 2006) (Fig. 2a). Toward the basin center in present-day northern Germany sediment source areas also include the Vindelician Massif, Bohemian Massif, Rhenish Massif, Pre-Carpathian Massif and London Brabant Massif (Röhling and Lepper, 2013) (Fig. 2). The sediment thickness and facies in this endorheic basin are distinctly different between the basin center and basin margin (Füchtbauer, 1967).

At the basin margin, fluvio-eolian, alluvial, and lacustrine deposits are dominant (Füchtbauer, 1967; Bourquin et al., 2009; Backhaus,

1974), whereas deposition in the basin center is dominated by overall finer grained lake margin, playa and locally shallow marine deposits (Füchtbauer, 1967; Leggewie et al., 1977), occasionally favoring conditions of ooid formation if carbonate-saturated water ingressed into the basin (Ziegler, 1982). Overall, the Buntsandstein in the studied marginal basin area in the state of Baden-Württemberg reaches thicknesses up to 500 m (Fig. 2b) (Nitsch, 2024). In the basin center thicknesses of the Buntsandstein generally range between 1000 and 1200 m, in tectonically active grabens (Glückstadt Graben and Horn Graben) thicknesses may reach up to 4000 m.

The Lower Buntsandstein (Induan-Olenekian) in the studied well from the Kraichgau region comprises the partially pebble-bearing sandstones of the Eck-Formation (suE) and pebble-bearing sandstones of the Badischer Bausandstein (sVs, Fig. 3a, b) (Nitsch, 2024). Where the Badischer Bausandstein is not pebble-bearing, it is assigned to the Miltenberg Fm. (suM). The Middle Buntsandstein (Olenekian-Anisian) contains several unconformities (Bachmann et al., 2010), highlighting the tectonic activity during the breakup of Pangea (Ziegler, 1990), while the sedimentary deposits record higher seasonal rainfall and progressing fluvial facies into the basin center. Three members (Lower, Middle, and Upper Geröllsandstein, sVgu, sVgm, sVgo), each separated by erosional surfaces can be subdivided in the studied well, which each show a fining upward sequence, and are intercalated with fine-grained clastic deposits (Aigner and Bachmann, 1992). They represent fluvio-eolian or fluvio-lacustrine deposits (Mader, 1982). The base of the Geröllsandstein sequence represents the base of an overall base level rise sequence extending further into the overlying fully marine Muschelkalk (Fig. 3c). Due to a shift from arid to semi-arid climate during the late Middle Buntsandstein, extensive dolomite-cemented soils are formed, which show a characteristic violet color in individual layers (Carnelian-Dolomite Horizon (belonging to sVK), Fig. 3a, b) (Mader, 1982). Due to an initial ingression of the alpine Tethys through the Silesian-Moravian and Carpathian gates during the Anisian Upper Buntsandstein, the basinal deposition is characterized by fossiliferous limestones, sandstones, and evaporites (Mader, 1982), whereas the marginal basin deposition is dominated by fine-grained fluvial sandstones of the Plattensandstein Formation (soPL) and playa-related siltstones and claystones of the Rötton Formation (soT, Schmidt et al., 2020). Overall, the main deposition of the Buntsandstein in the marginal facies is characterized by braided fluvial channels, dry to wet sandflat (also characterized as hybrid sand sheets), individual eolian beds, playa margin and playa deposits (Bourquin et al., 2009; Mader, 1982; Bofill et al., 2024). The transition to the Anisian to Ladinian Muschelkalk is marked by the last occurrence of red claystones called Grenzletten, from which on extensive marine limestone and evaporite sequences are formed in the region (Aigner and Bachmann, 1992; Geyer and Gwinner, 2011). The overlying Ladinian to Rhaetian Keuper is characterized by continental and marine deposits, including evaporitic claystones, dolomites, marls, and sandstones of playa lake, playa margin or fluvial origin (Geyer and Gwinner, 2011; Reinhardt and Ricken, 2000; Duringer et al., 2019).

Mesozoic subsidence continued until the Cretaceous and led to the deposition of marine Jurassic claystones, limestones, and sandstones (Bossennec et al., 2021; Böcker and Littke, 2015). Burial model reconstructions require additional Cretaceous deposits on top of the preserved sequence to match vitrinite reflectance values in the Heidelberg and Sexau areas (Böcker, 2015; Bossennec et al., 2015). Heterogeneous uplift from the Upper Cretaceous to Early Eocene resulted in a younging of strata in the subcrop of the base Eocene unconformity from north to south in the URG (Böcker, 2015; Schumacher, 2002). Whereas lithologies in the URG experienced another phase of subsidence, areas located on the Graben shoulder were not buried to great depths again since the Eocene formation of the URG (Bossennec et al., 2021; Bauer, 1994) (Fig. 2c).

3. Materials and methods

In total, 40 plug samples were retrieved from the Lower Buntsandstein section of the Kraichgau-1002 core material (509 – 708 m present-day depth). Samples were taken approximately every 5 m (average: 5.1 m) while also targeting the present lithofacies, resulting in individual intervals from 2.6 to 8.5 m. During sampling, lithofacies classification was done based on Miall (1978). The 2.54 cm (1 inch) plug samples were cut to length and dried at 40 °C in a vacuum oven for 72 h. The trim ends were used for thin section preparation. Trim ends were embedded in blue-dyed epoxy resin to highlight porosity, fixed on a glass slide and ground to ~30 μm thickness. Thirty-seven of these samples are polished, while three samples are stained using a combined Alizarin Red S and potassiumferricyanide staining solution in 0.3% HCl (Dickson, 1965) to aid the identification of carbonate cement phases for staining colors, see (Ölmez et al., 2024; Greve et al., 2024).

Porosity and density measurements were performed on the dried plug samples in a micromeritics He-pycnometer (AccuPyc II 1340) (Schmidt et al., 2020), Klinkenberg-corrected air permeabilities were measured in an air permeameter manufactured by Westphal Mechanik (Monsees et al., 2021). Permeability measurements are performed at steady-state flow rates at a confining pressure of 1.2 MPa. The lower measurement limit is at 0.0001 mD, values below that are plotted at 0.0001 mD, while the upper measurement limit is 10,000 mD. The reproducibility of permeability measurements is within an average of 1.8 % of the given values (Greve et al., 2024). The reproducibility of porosity measurements is within an average of 0.045 % of the given value. Measurement error bars are thus smaller than the plotted datapoints and are therefore omitted.

Point-counting was performed to assess the detrital and authigenic mineralogy and to assess optical porosity. Using a semi-automatic Pelcon point-counting stage mounted on a Leica DMLP microscope equipped with a Jenoptik Gryphax Subra camera, 300 points are counted per sample on a grid adjusted to the maximum observed grain size, to gain

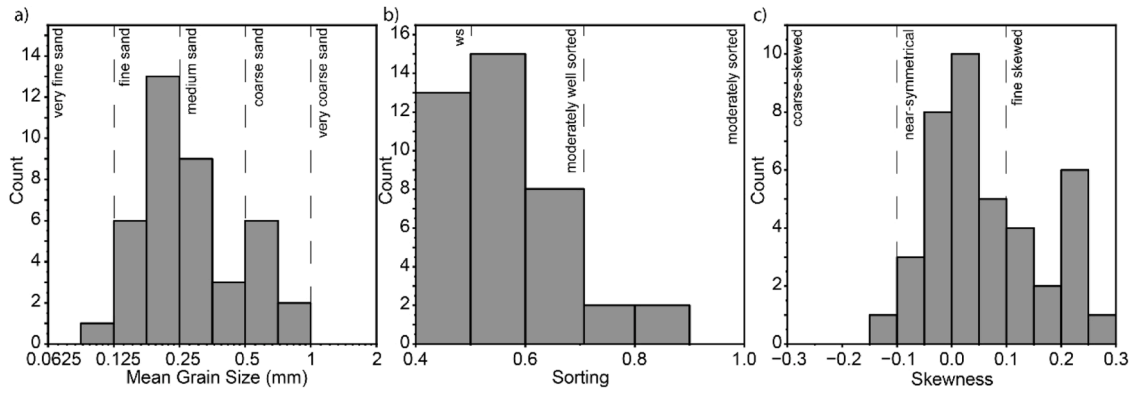

Fig. 4. Histograms showing a) the mean grain sizes, b) sorting, and c) skewness of the grain size distribution of the studied samples. ws: well sorted.

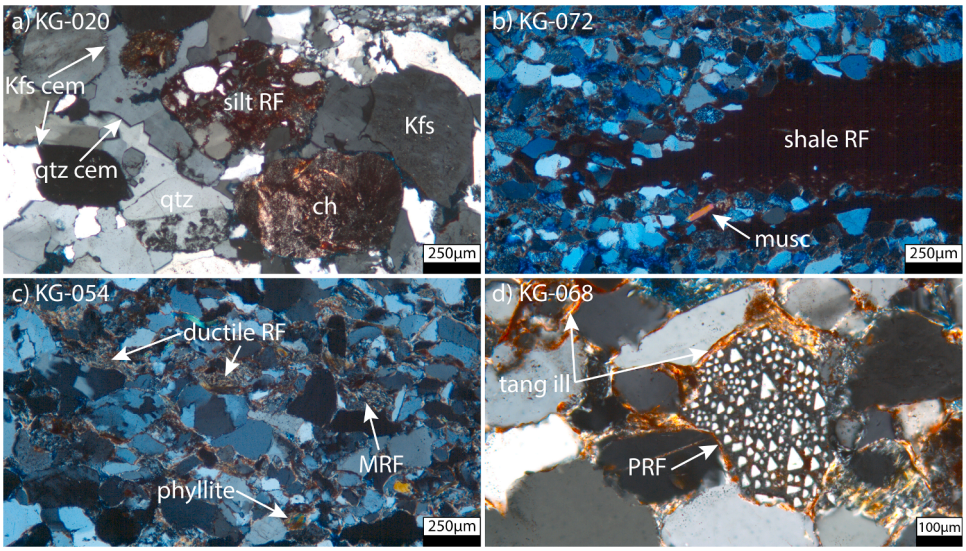

Fig. 5. a) Detrital quartz, K-feldspar, chert, siltstone rock fragments encased in quartz cement. b) Shale RF and muscovite flake. The more rigid quartz grains are deforming the margin of the shale RF. c) Ductile RF, phyllite, and MRF squeezed in between more rigid quartz and feldspar grains. d) Plutonic RF in between quartz grains.

area-weighted results (Busch et al., 2017). Grain sizes are measured on thin section photographs as the long axis of at least 100 grains per sample on a grid adjusted to the maximum observed grain size to gain area-weighted results. Sorting characteristics, skewness, and kurtosis are calculated according to Folk and Ward (1957) based on the grain size distribution. The detrital composition of sandstones is plotted according to Folk (1980). Based on the point-counting results, the intergranular volume (IGV) is calculated according to Paxton et al. (2002) as the sum of intergranular porosity, intergranular cements, and depositional clay mineral matrix. Compactional and cementational porosity loss is calculated according to Lundegard (1992) using an initial porosity of 45 % for fluvial deposits.

Grain coating coverages are differentiated as grain-to-IGV (GTI) and grain-to-grain (GTG) (Fig. 1) coating coverages according to Monsees et al. (2020)) using calibrated comparator images. Comparator images were evaluated using ImageJ by measuring the contact length between detrital grains covered by illite and relating it to the overall contact length between the two detrital grains, giving the GTG coating coverage. The GTI coating coverage is determined by measuring the length of illite-coated quartz grain surface in contact with the IGV and relating it to the total outline length of quartz grains in contact to the IGV (see also Busch et al., 2024). All sample data is provided in supplementary materials I.

During reservoir quality rock typing, the classification of two distinct subsets of samples was additionally confirmed using k-means clustering analyses performed in OriginPro based on the petrographically determined properties.

4. Results

4.1. Texture and structure

The studied samples are classified as very fine-grained sandstone ($N = 1$), fine-grained sandstone ($N = 19$), medium-grained sandstone ($N = 12$), and coarse-grained sandstone ($N = 8$) (Fig. 4a, mean grain size range: 0.107 – 0.852 mm). Samples are well sorted ($N = 13$), moderately well sorted ($N = 23$), and moderately sorted ($N = 4$) (Fig. 4b). Mostly, samples' grain size distributions are near-symmetrical ($N = 26$) with only 13 samples being fine-skewed and one sample being coarse-skewed (Fig. 4c).

The retrieved plug samples originate from the following lithofacies:

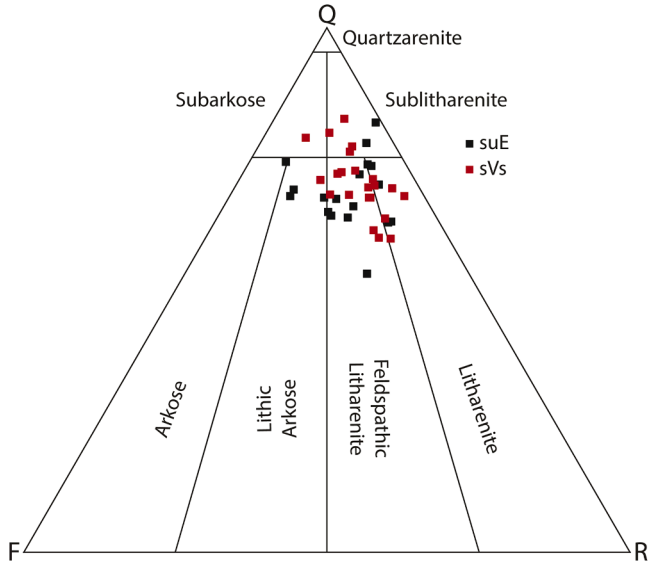

Fig. 6. The studied samples are classified as litharenite, feldspathic litharenite, lithic arkose, subarkoses, and sublitharenites. The two studied formations do not show distinct compositional differences.

massive sandstones (Sm, $N = 8$), planar cross-laminated sandstones (Sp, $N = 7$), trough cross-bedded sandstones (St, $N = 8$), horizontally laminated sandstones (Sh, $N = 13$), and ripple laminated sandstones (Sr, $N = 4$).

4.2. Detrital composition

The most abundant detrital constituent based on point-count analyses is quartz (incl. mono-, poly- and undulose quartz grains, Fig. 5a) with an average of 52 % (range: 38.3–66.7 %, supplementary materials 1, Fig. 7a). Rock fragments (RF) are the second most frequently occurring grain type with 15.7 % on average (range: 0.7–60.3 %). With an average of 7.8 % (range: 0.7–14.0 %) feldspar appears exclusively as K-feldspar which also appear partially dissolved containing intragranular porosity (Fig. 5a).

Rock fragments include chert, (avg.: 4.7 % range: 0.7–14.3 %,

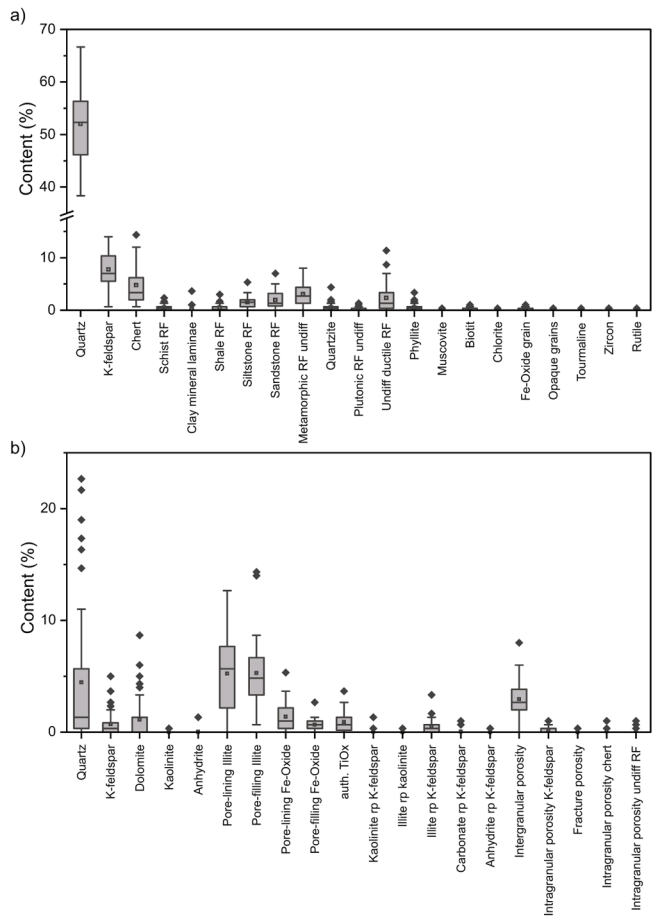

Fig. 7. Box-Whisker plots of a) the detrital and b) the authigenic mineral contents of the 40 studied samples.

Fig. 5a), undifferentiated metamorphic rock fragments (MRF, avg.: 3.0 %, range: 0.0–8.0 %, Fig. 5c), ductile RF, (avg.: 2.4 %, range: 0.0–11.3 %, Fig. 5c), sandstone RF (avg.: 1.9 %, range: 0.0–7.0 %), siltstone RF (avg.: 1.5 %, range: 0.0–5.3 %, Fig. 5a), quartzite (avg.: 0.5 %, range: 0.0–4.3 %-), phyllite (avg.: 0.5 %, range: 0.0–3.3 %, Fig. 5c), schist (avg.: 0.5 %, range: 0.0–2.3 %), shale (avg.: 0.4 %, range: 0.0–3.0 %, Fig. 5b), and plutonic RF (avg.: 0.3 %, range: 0.0–1.3 %, Fig. 5d). Undifferentiated ductile rock fragments contain grains, which are deformed in between more rigid grains, which omits an identification of the original detrital grain type. In addition to the undifferentiated ductile rock fragments, chert, shale, phyllite, schist, and sheet silicate-rich metamorphic rock fragments also often appear deformed in between detrital quartz grains (Fig. 5b and c) and are combined as ductile grains for further rock typing.

According to the sandstone classification of Folk (1980), samples are classified as litharenite, feldspathic litharenite, lithic arkose, subarkoses, and sublitharenites (Fig. 6). No distinct differences between the studied formations (suE and sVs) can be seen with regard to their detrital composition.

Tangential illite, encasing detrital grains, is present at grain contacts and appears with an average of 5.3 % (range: 0–12.7 %; Fig. 5d). Other detrital components are iron oxide (FeOx-) grains (0.2 % on average), biotite (0.1 % on average), clay mineral laminae (0.1 % on average), muscovite (0.07 % on average), rutile (0.04 % on average), chlorite (0.03 % on average), tourmaline (0.03 % on average), opaque grains (0.02 % on average) and zircon (0.01 % on average).

4.3. Authigenic components

The most prominent authigenic component based on point-counting analyses is radial and meshwork illite that is on average present with 5.3 % (range: 0.7–14.3 %, Fig. 7b) radially encasing detrital grains (Fig. 8a and g) or filling intergranular pores. Radial illite is observed to form directly on the detrital grain surfaces or may precipitate on pre-existing tangential illite, growing into the pore space and possibly resulting in pore-bridging textures close to pore throats (Fig. 9e). Radial illite is only observed at the interfaces of detrital grains with the IGV. Meshwork illite mostly fills intergranular pores and appears fiber-like and pore-bridging in thin sections. Meshwork and pore-bridging illite are occasionally encased in the outer margins of quartz overgrowth cements (Fig. 8i).

Additionally, dissolved grains, especially feldspars (Fig. 8c, e, h) and rock fragments containing feldspar minerals are filled with replacive illite (avg.: 0.5 %, range: 0.0–3.3 %) (Fig. 8c). Illite that replaces feldspar still resembles the cleavage planes of the original K-feldspar grains (Fig. 8c) and rarely replaces kaolinite that initially replaced the feldspar grains (avg.: <0.1 %, range: 0.0–1.3 %). Rarely kaolinite is also observed in intergranular pores (avg.: <0.1 %, range 0.0–0.3 %).

The second-most prominent authigenic constituent that can pervasively fill pore spaces in some samples is syntaxial quartz overgrowth cement that is on average present with 4.5 % (Fig. 8a, f, h). The amount of quartz cement varies greatly (0.0–22.7 %) throughout the studied sample series. Where tangential and radial illite as well as well-developed hematite rims are continuously surrounding the quartz grains, syntaxial quartz cement is observed to occur in smaller quantities or to be absent (compare Fig. 9b, e, f).

The detrital tangential illite rims are often associated with pigmented hematite dust rims or are completely stained red by hematite which also rims detrital grains (avg.: 1.4 %, range: 0.0–5.3 %) (Fig. 9c, d). Rarely, hematite appears pore-filling (avg.: 0.7 %, range: 0.0–2.7 %).

Syntaxial feldspar overgrowth cementation (avg.: 0.7 %, range: 0.0–5.0 %) shows either syntaxial facets encased in dolomite or quartz cements (Fig. 8f), or shows compromise boundaries with quartz cements (Fig. 8h). In areas where radial illite rims are not completely encasing detrital feldspar grains, syntaxial feldspar cements precipitate on the uncoated feldspar grain outlines.

Dolomite cement is present in the studied samples with an average of 1.1 % (range: 0–8.7 %) and is either observed as localized nodules with a poikilotopic texture, encasing detrital grains and preserving a floating grain texture (Fig. 8d), or fills residual pore spaces in compacted sediments, also encasing syntaxial quartz or feldspar cements (Fig. 8a, b). Furthermore, dolomite is observed to fill the intragranular porosity in feldspar(-containing) grains and cherts (avg.:<0.1 %, range 0.0–1.0 %) (Fig. 8e). In a stained sample, the nodular dolomite is outlined by a thin rim of ferroan dolomite (pale blue, Fe-dolomite), which is itself again partially encased in rhomb-shaped siderite precipitates (rusty brown color in ppl, Fig. 8b). Both of the latter carbonate cement phases were not encountered during point-counting. The nodular dolomite cements also exhibit two distinctly different paragenetic relationships to encased grains. In the center of the nodule, dolomite mostly encases detrital quartz grains without a syntaxial overgrowth or grain coating phase (Fig. 8d), whereas the quartz grains at the margin of the nodule can contain syntaxial quartz overgrowths or radial illite rims (Fig. 8a, d, j). Therefore, two generations of dolomite cement precipitation are interpreted (dol I and II).

Authigenic Ti-oxides (TiOx) range from 0.0 to 3.7 % (avg.: 0.9 %, Fig. 8c and g). They appear encased by syntaxial quartz cement (*Fig. 8g*), at the margin inside dolomite nodules (Fig. 8j), between compacted grains in intergranular pores, and within dissolved K-feldspar together with replacive illite and kaolinite phases (Fig. 8c). Authigenic Ti-oxides are also prominently observed in between radial illite crystals and in close spatial association to biotite (*Fig. 8g*). The TiOx appear as small isotropic crystals dispersed in the pore space.

In one sample, anhydrite cement (avg.: <0.1 %, range: 0.0–1.3 %)

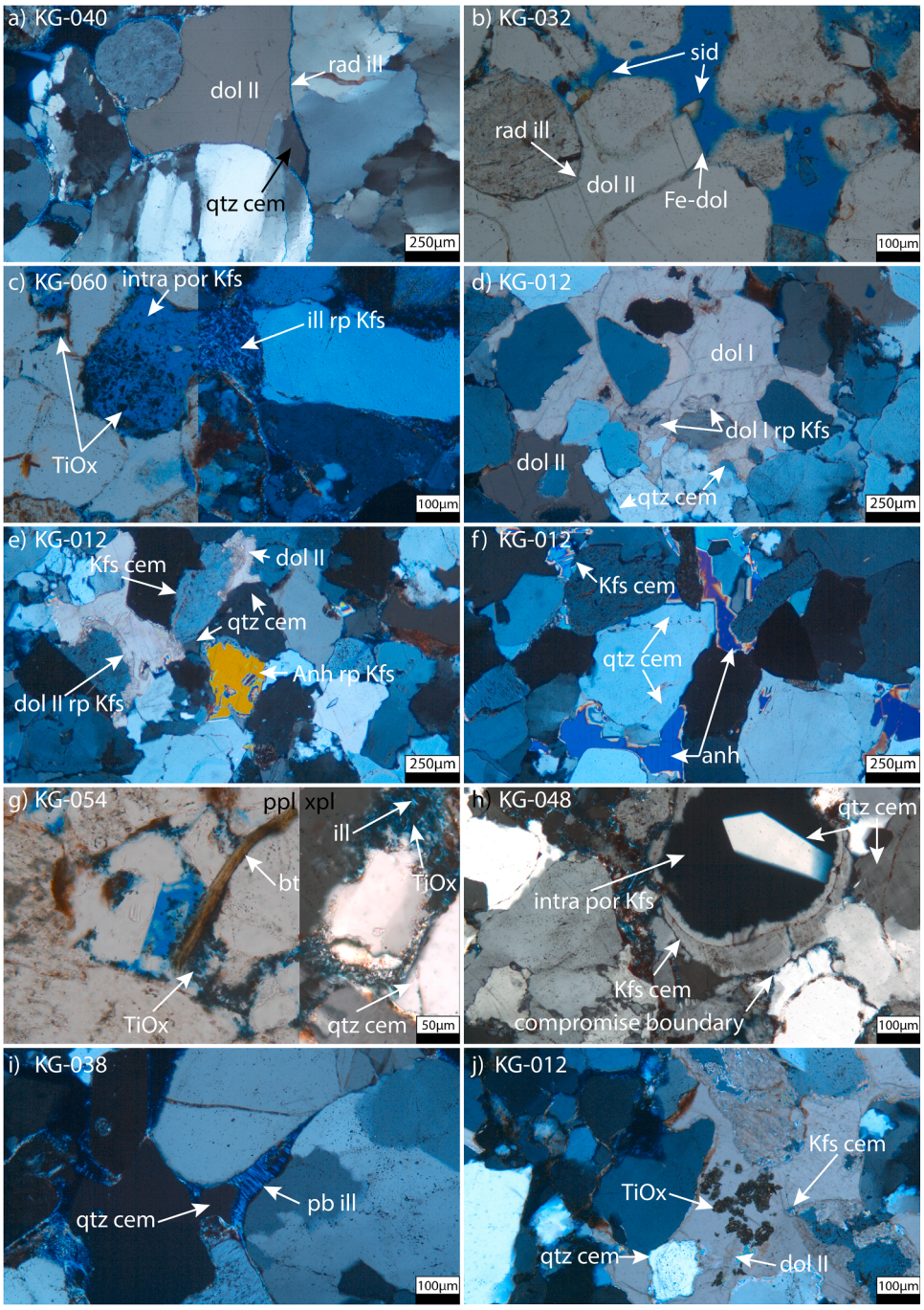

Fig. 8. a) Radial illite encased by dolomite (dol II), which also encases syntaxial quartz overgrowth cements. b) Margin of a dolomite nodule (dol II) overgrown by Fe-dolomite (stained blue) and siderite. c) Intragranular dissolution porosity in K-feldspar grain filled by replacive illite and TiOx crystals. The TiOx crystals are also present in between radial illite rims. d) Dolomite nodule, where in the center (dol I) a floating grain texture is preserved, whereas toward the margin a second dolomite texture (dol II) also encases quartz grains including a syntaxial overgrowth cement. e) Dolomite and anhydrite replacing partially dissolved K-feldspar grains. f) Anhydrite cement encasing euhedral quartz and K-feldspar overgrowth cements. g) TiOx crystals in the vicinity of biotite flake and intergrown with radial illite coatings and encased in quartz cement. h) Intragranular dissolution porosity in K-feldspar grain partially filled by quartz outgrowth. The original K-feldspar grain still preserved the syntaxial K-feldspar overgrowth with a compromise boundary with syntaxial quartz cement. i) Pore-bridging illite which is marginally encased in quartz cement. j) TiOx encased in dolomite cement (dol II), which also encases quartz overgrowths and replaces and encases K-feldspar grains including a euhedral overgrowth cement.

was observed and occurs either in small intergranular pores or more pervasively filling intergranular pores and dissolved K-feldspar and rock fragments (avg.:<0.1 %, 0.0–0.3 %, Fig. 8e). Anhydrite cement encases syntaxial quartz overgrowth cement and K-feldspar cement, both showing euhedral crystal faces (Fig. 8f).

4.3.1. *Optical porosity*

Optical porosity (i.e., porosity from point-counting) is present as either intergranular porosity (avg.: 3.0 %, range: 0.0–8.0 %), intragranular porosity in either K-feldspar grains (avg.: 0.2 %, range: 0.0–1.0 %), chert (avg.: <0.1 %, range: 0.0–1.0 %), or undifferentiated RF (avg.: 0.1 %, range: 0.0–1.0 %). In one sample fracture porosity (0.3 %) was

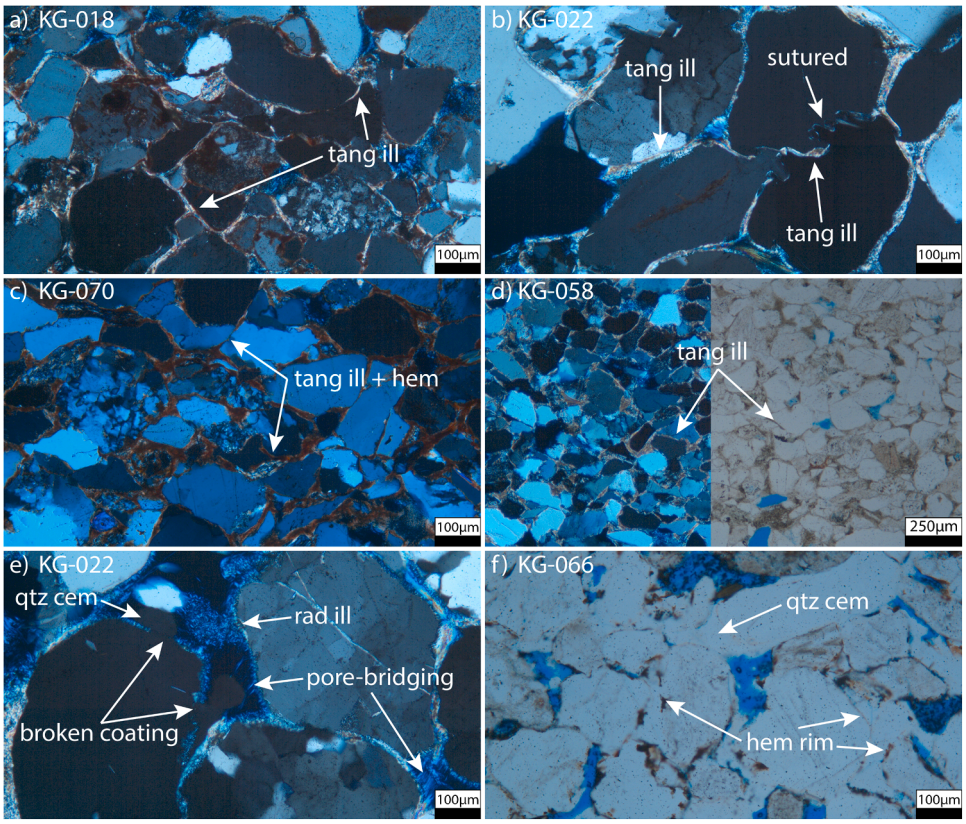

Fig. 9. a) Tangential illite grain coatings. b) Tangential illite grain coatings and sutured grain contacts. c) Hematite stained tangential illite grain coatings. d) Unstained tangential illite rims. e) Radial illite grain coatings, occasionally developing a pore-bridging texture. Where the grain coating coverage is incomplete, syntaxial quartz cement can precipitate. f) Pigmented and more continuous hematite rims encased in syntaxial quartz cement. cem: cement, ill: illite, tang: tangential, rad: radial.

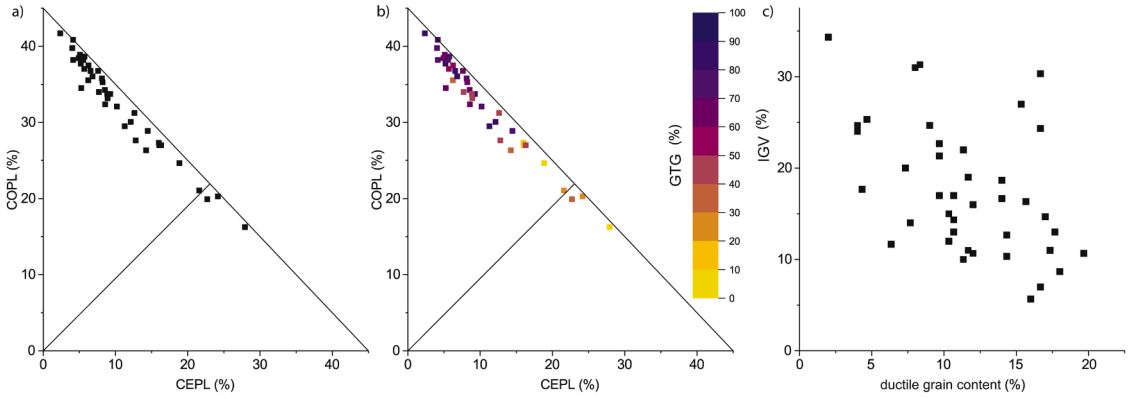

Fig. 10. a) Most of the studied samples show a compaction dominated porosity loss. b) Samples with a high GTG coating coverage show the highest compactional porosity loss. c) An increase in the ductile grain contents poorly correlates negatively with the IGV.

observed. Total optical porosity ranges from 0.0 to 8.3 %, with an average of 3.3 %.

4.4. Compaction and porosity loss

The IGV, as an indicator for compaction, ranges from 5.7 to 34.3 % (avg.: 17.7 %) (supplementary materials I). The IGV only shows a poor negative correlation with the ductile grain content (R^2=0.22, Fig. 11c). The compactional porosity loss (COPL) ranges from 16.2 to 41.7 % (avg.: 32.7 %) (Fig. 10a), while the cementational porosity loss (CEPL) only ranges from 2.3 to 27.9 % (avg.: 10.3 %).

4.5. Grain coatings

The main grain coating phases are tangential (Fig. 9a–d) and radial illite (Fig. 9e), as well as hematite (Fig. 9f). Hematite mainly occurs as pigmented dust rims on quartz grains (Fig. 9f), extensively covering the initial grain outline, or staining the tangential illite rims (Fig. 9c). Tangential illite may also occur as an unstained mineral phase (Fig. 9d). Radial illite, oriented perpendicular to the grain surface, grows into the pore space, occasionally forming a pore-bridging texture (Fig. 9e). All three grain coating textures and minerals are included in the assessment of the GTI coating coverage. For the GTG coating coverage, only tangential illite is considered, as radial illite is not observed at grain

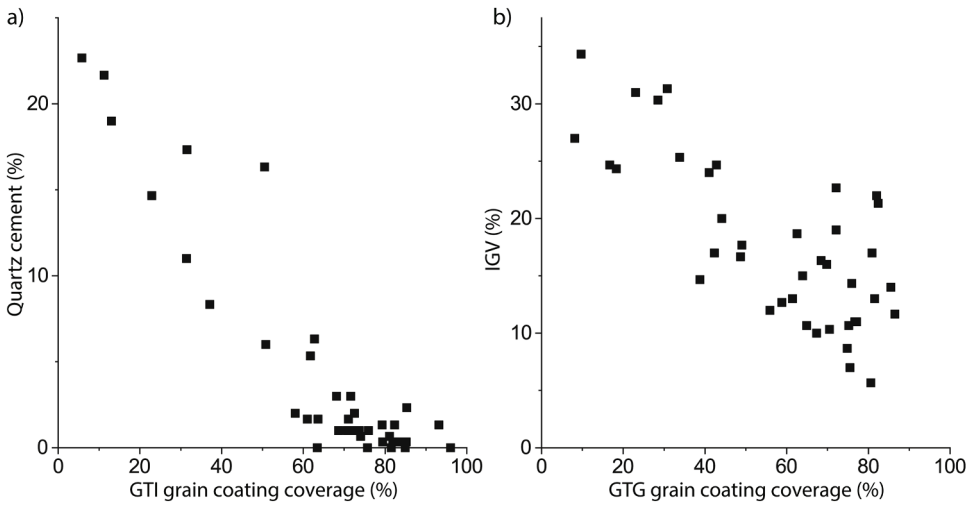

Fig. 11. a) An increase in GTI coating coverage negatively correlates with syntaxial quartz cement contents. b) An increase in GTG coating coverage negatively correlates with the IGV.

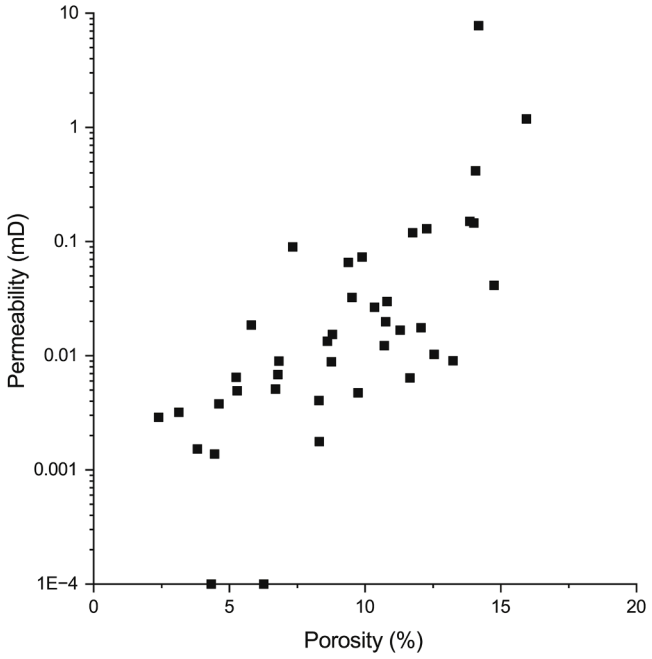

Fig. 12. Porosity-permeability cross plot.

contacts.

The GTI coating coverage ranges from 5.8 to 96 % (avg.: 65.1 %) and shows a negative correlation with the amount of syntaxial quartz cement contents (Figs. 9c, e and 11a, R^2=0.84). GTG coating coverages range from 8.1 to 86.5 % (avg.: 57.5 %) and show a negative correlation to the IGV (Fig. 11b, R^2=0.56). In samples with large GTG coating coverages, this effect is also represented in form of sutured grain contacts covered by illite (Fig. 9b).

4.6. Porosity and permeability

Porosity of the studied samples ranges from 2.4 – 16.0 %, with permeability ranging from 0.0014 to 7.7 mD, with two samples below the measurement limit (<0.0001 mD) (Fig. 12a). Overall, porosity and permeability show a general positive correlation, where samples with higher porosity generally have higher permeabilities. However, with average permeabilities of 0.28 mD and average porosities of 9.2 %, reservoir quality is poor.

4.7. Rock typing

Color coding porosity-permeability cross plots for petrographic properties allows the delineation of controlling factors on reservoir quality (RQ) (Fig. 13).

When assessing the influencing factors, it becomes apparent that the sample series can be divided into two separate classes. For simplicity, only one class is outlined by a dashed line (class I), all other samples belong to the other class (class II).

The IGV shows a variable influence on RQ, as the lowest porosity and permeability values are recorded in samples having the lowest IGV (Fig. 13a), while at moderate porosity (5–12.5 %) samples that show higher IGV (>20–25 %) have higher permeabilities, than samples with lower IGV (<25 %). Samples showing the highest porosities and permeabilities have moderate IGV values between 10 and 30 %.

The subdivision into two classes becomes obvious when assessing the COPL and CEPL (Fig. 13b and c). At the same porosities (5–12.5 %), samples with lower COPL (<30 %, class I) show higher permeabilities than samples with higher COPL (mostly >30 %) (Fig. 13b). For samples from class II a general decrease in porosity with an increase in COPL can be observed (Fig. 13b). This assessment is supported by analysis of Box-Whisker plots (Fig. 14b), where a general decrease in porosity can be observed above a COPL of 30 %. Similarly, the permeability generally decreases above a COPL of 20 % (Fig. 14e). The opposite can be seen for the CEPL (Fig. 13c). At the same porosities (5–12.5 %) samples, which experienced a higher CEPL (>15 %, class I) show higher permeabilities than samples which experienced a lower CEPL (<15 %). For the remaining samples of class II, the correlation to the CEPL remains indistinct, while the lowest CEPL values correspond to lowest porosities. When assessing the Box-Whisker plots a general increase in porosity (Fig. 14a) and permeability (Fig. 14d) can be associated to an increase in CEPL.

Color-coding for the GTG coating coverage again shows samples of class I (GTG <50 %) behaving differently than samples of class II (GTG >40 %). Lower GTG coating coverages of samples in class I result in higher permeabilities at porosities between 5–12.5 %. Samples of class II show a general decrease in porosity with an increase in GTG coating coverage. This is also observed when assessing the tangential illite content, which is the grain coating mineral phase at grain contacts, where highest porosities and permeabilities are observed in samples containing small tangential illite contents (Fig. 14c and f).

There appears to be no difference in the ductile grain content of

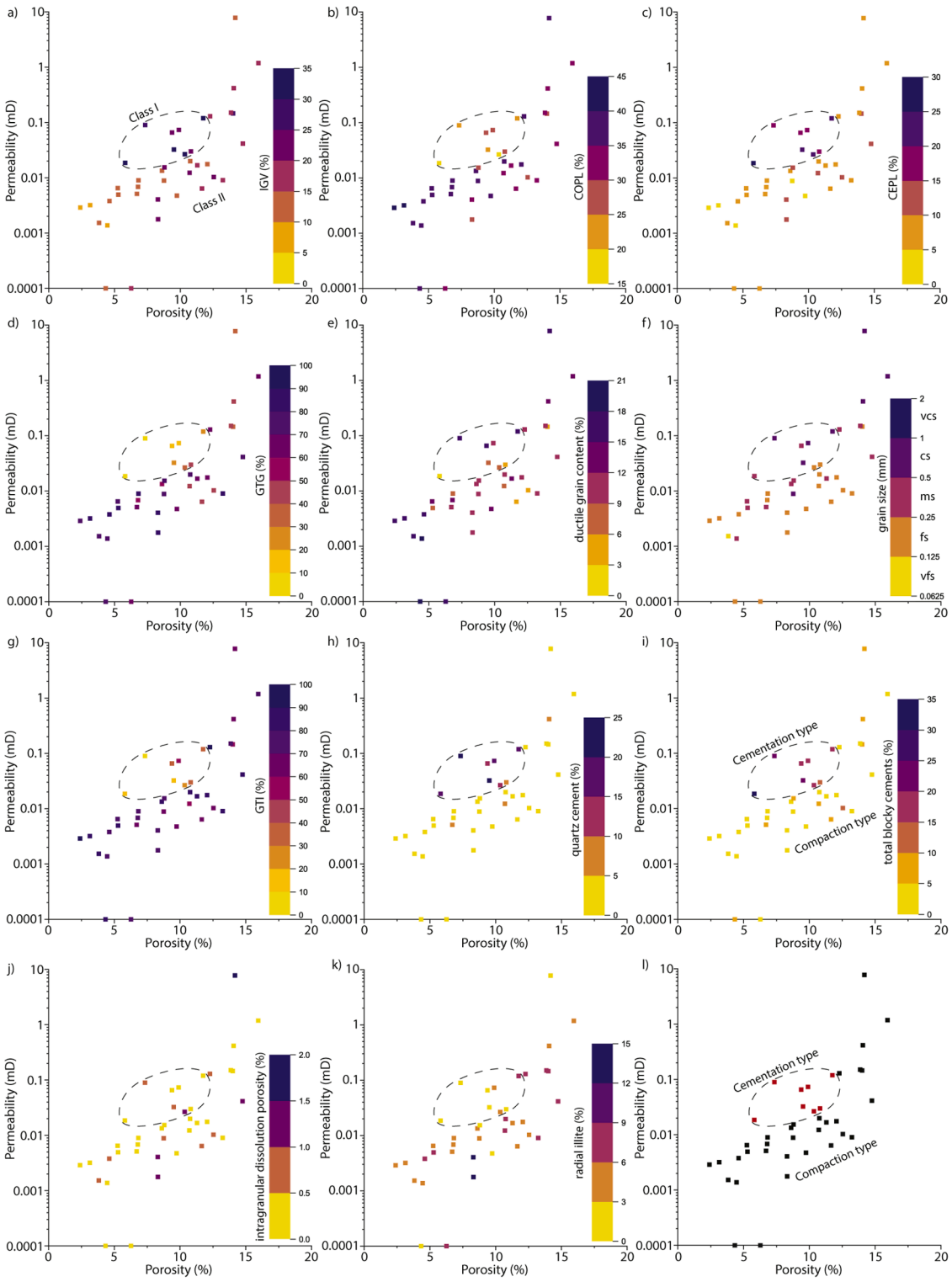

Fig. 13. Porosity-permeability cross plot color coded for: a) IGV, b) COPL, c) CEPL, d) GTG coating coverage, e) ductile grain content, f) detrital grain size, g) GTI coating coverage, h) quartz cement content, i) total blocky cement content (Sum of quartz, feldspar, dolomite, and anhydrite cements), j) intragranular dissolution porosity, k) radial illite content, and l) the result from k-means cluster analysis.

samples from both classes (Fig. 13e) with only some samples containing >18 % ductile grains having lowest permeabilities (0.001–0.0001 mD). When assessing the effect of the detrital grain size, it becomes apparent, that generally samples with larger detrital grain sizes show higher permeabilities at the same porosity than samples with smaller detrital grain size (Fig. 13f).

Samples with a lower GTI coating coverage (generally <60 %, class I) show higher permeabilities at porosities between 5–12.5 %. Samples of class II have generally higher GTI coating coverages (>60 %) (*Fig. 13g*). As the GTI coating coverage also correlates with the syntaxial quartz cement contents, samples of class I with low GTI coating coverages show higher quartz cement contents than samples of class II. Samples with

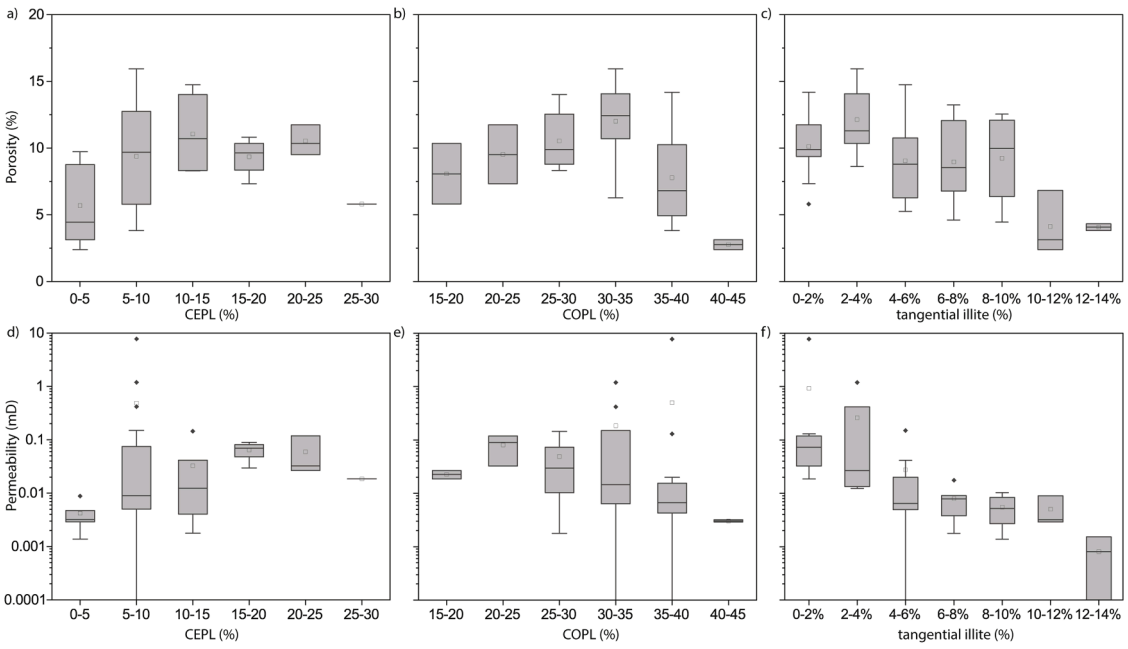

Fig. 14. Box-Whisker plots comparing the CEPL and porosity (a), or permeability (d), the COPL and porosity (b), or permeability (e), and the tangential illite content and porosity (c), or permeability (f).

higher quartz cement contents are characterized by higher permeabilities in the porosity range of 5–12.5 %, than samples with lower quartz cement contents in the same range (Fig. 13h). A similar effect can be seen when assessing the influence of the total blocky cement content (quartz-, K-feldspar-, dolomite-, and anhydrite cements, Fig. 13i). Samples with higher blocky cement contents are characterized by higher permeabilities in the porosity range of 5–12.5 %, than samples with lower blocky cement contents in the same range (Fig. 13i).

The sample with the highest intragranular dissolution porosity (2.0 %, in K-feldspars, chert, and undifferentiated RF, Fig. 13j) is the most permeable sample. Other samples containing 1.0–1.5 % intragranular dissolution porosity however, are found in samples with lower He-porosity (~8.3 %) and much lower permeability (between 0.001–0.01 mD). The same two samples are also characterized by the highest radial illite contents (12–15 %, Fig. 13k) further reducing permeability.

The two defined classes are also obtained when performing a k-means clustering analysis on porosity, permeability, IGV, COPL, CEPL, GTI coating coverage, quartz cement content, and blocky cement content data (Fig. 13l). Samples of class I can be assigned to show RQ controls mostly driven by cementational processes (cementation type) as cementation rather preserves permeability, when assessing the porosity range between 5–12.5 % (Fig. 13c, h, i) largely related to GTI coating coverages (Figs. 11a and 13g). Conversely, samples of class II show that RQ is mostly controlled by compactional processes, highlighted by the correlation with the IGV and COPL (Fig. 13a and b). Compaction is enhanced by elevated GTG coating coverages and in individual samples by the elevated ductile grain content (Figs. 10b, 11b, 13d, e).

4.7.1. *Relation of grain coating properties and permeability to grain sizes*

The main controls on RQ are related to the detrital grain size, quartz cement, and grain coating coverage, the latter composed of tangential and radial illite grain coatings (Fig. 13). As grain coating coverages (GTI and GTG) have already been linked to compaction and quartz overgrowth cementation, the main focus of this chapter is on the relation of grain coating characteristics and permeability to detrital grain sizes of the studied samples and available published datasets from core material (Busch et al., 2022a; Busch et al., 2024; Quandt et al., 2022; Busch et al., 2022b).

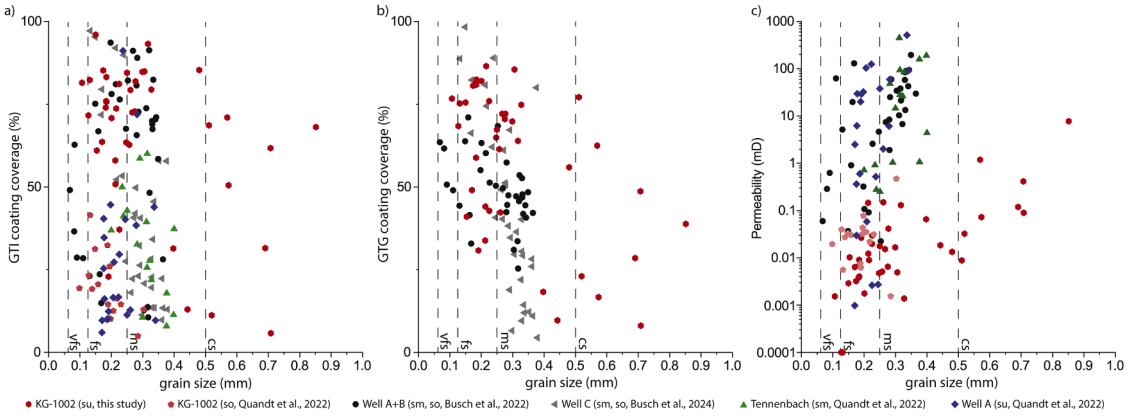

Fig. 15. a) Relation of grain size and grain-to-IGV (GTI) coating coverage. b) Relation of grain size and grain-to-grain (GTG) coating coverage. c) Relation of grain size and permeability. vfs: very fine sand, fs: fine sand, ms: medium sand, cs: coarse sand, su: Lower Buntsandstein, sm: Middle Buntsandstein, so: Upper Buntsandstein. (Additional data from Busch et al. (2022a, 2024) and Quandt et al. (2022)).

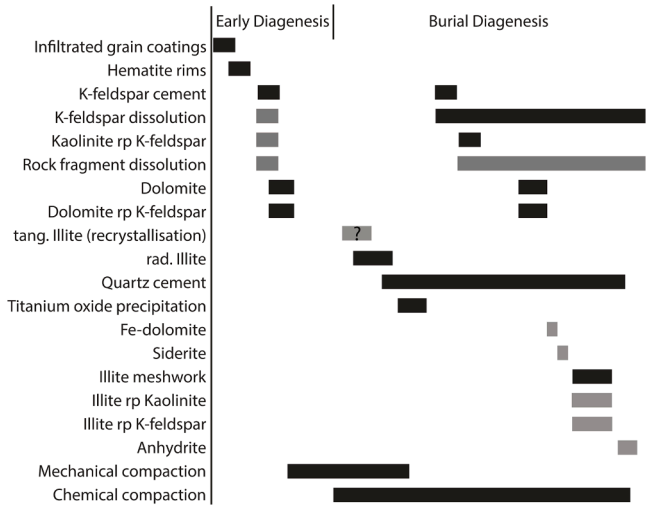

Fig. 16. Paragenetic sequence of the authigenic mineral formation in the studied well section. rad: radial, rp: replaces, tang: tangential. Grey boxes indicate this process was only observed in individual samples, the question mark indicates possible alterations.

When assessing the relation of grain coating coverages (GTI and GTG) and grain size, no consistent correlation for samples from this and other available cores from the Buntsandstein can be established (Fig. 15a and b). The coefficients of correlation are very low (R^2<0.01 for GTI coating coverages and R^2=0.19 for GTG coating coverages). While, across individual sample series a positive correlation between grain sizes and enhanced permeability could be established (this study, Fig. 15c) no correlation can be established if other available core sample are included (R^2=0.05, all samples, Fig. 15c).

5. Discussion

5.1. Paragenetic sequence

The paragenetic sequence derived for the studied well section is comparable to other previously published sequences in the marginal facies of the Buntsandstein within the Germanic Basin (Busch et al., 2024; Quandt et al., 2022; Bossennec et al., 2021; Schmidt et al., 2020; Busch et al., 2022b; Soyk, 2015) however, some location specific alterations are observed.

5.1.1. Early diagenesis

As pigmented hematite rims are encased in syntaxial quartz cements, are present at grain contacts (Fig. 9f), and stain the detrital or syndepositional tangential illite rims (Fig. 9c), they are interpreted to be the earliest diagenetic alteration. This generally fits the formation time derived from other red bed deposits from arid or semi-arid depositional settings (Walker, 1967) as an alteration product from Fe-rich alumosilicates. The hematite rims and hematite-stained tangential illite rims are often observed to be thicker in grain indentations (Fig. 9f), whereas they are absent at grain protrusions, which has previously been related to grain remobilization in non-stabilized fluvio-eolian deposits (Ajdukiewicz et al., 2010). Therefore, they may theoretically be considered as part of the detrital grains at the time of deposition. However, some samples show hematite stained tangential illite completely encasing the grain outlines, therefore grain remobilization only affected individual samples. For the sake of simplicity, these processes are not differentiated for the paragenetic sequence (Fig. 16).

Syntaxial K-feldspar overgrowth cements, encasing pigmented hematite rims (Fig. 8e and f), are encased in dolomite nodules and quartz cement (Fig. 5a), thus an early diagenetic formation is interpreted. A possible intraformational source for K-feldspar cements is the partial dissolution of detrital K-feldspar grains, which are also filled by nodular dolomite cements (Fig. 8d). An early diagenetic K-feldspar cement generation in the Buntsandstein from the URG and the western graben shoulder was also observed by Bossennec et al. (2021) and dated using the $^{40}Ar/^{39}Ar$ method. The early diagenetic dissolution of K-feldspar and subsequent precipitation of syntaxial cements was also observed in Permian Rotliegendes deposits, also formed in an arid to semi-arid depositional environment, from the Netherlands (Gaupp and Okkerman, 2011; Amthor and Okkerman, 1998). The alteration of detrital feldspar grains also produces kaolinite, which is present in deformed intragranular pores, where surrounding rigid grains indent the original feldspar grain outline (Fig. 8c), indicating that the intragranular porosity formed prior to the onset of mechanical compaction.

As dolomite cemented nodules (dol I) preserve a floating grain texture, where detrital grains are not in contact with each other (Fig. 8d), their formation is interpreted to pre-date the onset of mechanical compaction. As the dolomite also encases K-feldspar cements and filling intragranular pores in partially dissolved K-feldspar grains, it syn- to postdates these processes. Similar interpretations are supported by results from the Buntsandstein in the Upper Rhine Graben area (Quandt et al., 2022) as well as Triassic samples from the UK (Lippmann, 2012) and Thuringia in Germany (Aehnelt et al., 2021). Previously their formation was interpreted as a pedogenic dolocrete (Aehnelt et al., 2021), which would fit into the semi-arid climate during deposition of the sandstones. Similar dolomite formation in Late Triassic (Carnian--Norian) sandstones in central-eastern France was linked to pedogenic/near-surface processes using U-Pb dating (Regnet et al., 2024).

5.1.2. Burial diagenesis

As syntaxial quartz overgrowth cements are absent on GTI interfaces covered by radial and tangential illite grain coatings, burial diagenetic alteration likely initiated with the precipitation of radial illite on detrital grain surfaces and tangential illite (Fig. 8a and 9e) prior to quartz cementation. Soyk (Soyk, 2015) found indications of illite/smectite mixed layer clays as grain coatings in samples from the Buntsandstein from southern Germany, implying a recrystallization of previous smectitic precursor coatings in the studied region and lithology. However, fluvial samples from recent fluvio-eolian deposits, that did not experience any burial diagenetic overprint, can also contain illitic grain coatings (Esch et al., 2008; Busch, 2020), highlighting that a smectitic grain coating precursor might not be necessary to form tangential and radial illitic coatings. Where tangential and radial illite grain coatings are not completely encasing grain surfaces, the coatings are marginally encased in quartz cement (Fig. 8a). The burial diagenetic formation of illite is also supported by K/Ar-age dating of illite in the Buntsandstein from the URG area by Clauer et al. (2008), which give age ranges from 210–155 Ma and 110–95 Ma, which, when correlated with burial and thermal reconstructions from the URG (Bossennec et al., 2021), correspond to temperature ranges between 56–102 °C and 115–117 °C, respectively. In samples, which are characterized by intense chemical compaction along tangential illite coated quartz grain interfaces, radial illite is mostly absent, indicating that porosity and permeability was already reduced in these samples at the time of radial illite precipitation.

As syntaxial quartz cements encase the radial illite coatings (Fig. 8a), quartz cements have to form during or after the precipitation of radial illite coatings. As the precipitation kinetics of quartz are temperature dependent (Lander et al., 1997; Walderhaug et al., 2000; Lander and Bonnell, 2008), a formation during burial diagenesis is likely. Based on the petrographic observations, the most likely source is either from the enhanced chemical compaction at tangential illite coated quartz grain contacts (Fig. 9b) (Heald, 1955), clay mineral alterations, K-feldspar dissolution (Lanson et al., 2002), or associated to the hydrothermal event, resulting in the precipitation of illite (Clauer et al., 2008).

As some syntaxial K-feldspar cements on (partially dissolved) grains show compromise boundaries to syntaxial quartz cement (Fig. 8h)

another phase of K-feldspar dissolution and precipitation is interpreted to coincide with the precipitation of quartz cements. As uncompacted intragranular porosity in K-feldspar grains is rarely filled by kaolinite, another minor phase of kaolinite authigenesis is interpreted. This is in general agreement with other studies from the region (Busch et al., 2022b).

As small anhedral TiOx particles are growing in between replacive kaolinite and radial illite (Fig. 8c and g) it is interpreted that it is syn- to postdating the feldspar replacement by kaolinite and radial illite precipitation. Furthermore, the TiOx particles are partly encased in syntaxial quartz overgrowth cements (*Fig. 8g*), indicating formation prior to or during quartz cementation. We interpret a relative age during burial diagenetic quartz cementation, while post-dating radial illite precipitation. This is generally in agreement with Morad and Aldahan (1987), who observed a similar paragenesis. They also observed TiOx authigenesis sourced by biotite (Morad and Aldahan, 1987), which was also observed in the studied samples (Fig. 8g). As the TiOx were also observed encased in dolomite at the margins of dolomite nodules (Fig. 8j), where dolomite also encases radial illite and syntaxial quartz cements (Fig. 8a, b, d), the TiOx precipitation furthermore has to predate the second phase of dolomite precipitation.

The second phase of dolomite cements (dol II) encases syntaxial quartz cements and radial illite rims (Fig. 8a and b), and therefore syn- to postdates the precipitation of these cements. The second phase of dolomite precipitation either syntaxially precipitates marginally on the early diagenetic dolomite nodules, or in compacted pores, where it is observed to replace K-feldspar grains and cements, while encasing quartz cements (Fig. 8e). As the second dolomite phase at the margin of dolomite nodules is itself syntaxially overgrown by a light blue-stained Fe-dolomite rim (Fig. 8b) whose euhedral facets are encased by siderite, a continuously more Fe-rich carbonate cement precipitation during burial diagenesis can be reconstructed, which is in agreement with previously studied carbonate cemented samples from the region surrounding and within the URG (Busch et al., 2022; Soyk, 2015).

As the meshwork and pore-bridging illite (Fig. 8e) is not observed to be encased in dolomite and only at the margins of quartz cements (Fig. 8i), its formation is interpreted to post-date dolomite II formation and syn-date burial diagenetic quartz cement precipitation (Fig. 8e). It is conceivable that this late stage of illite authigenesis corresponds to the younger illite authigenesis around 110–95 Ma derived by Clauer et al. (2008). It is interpreted that the authigenic kaolinite and feldspar were also replaced by illite during this phase, although a replacement during the earlier radial illite precipitation phase is also possible. However, replacive illite (or kaolinite) was not observed to be present in K-feldspar grains which have been (partially) replaced by dolomite cement.

As anhydrite cement fills intergranular pores encasing euhedral quartz overgrowth cements (Fig. 8f) and fills intragranular pores after K-feldspar dissolution (Fig. 8e), it is interpreted to be a late burial diagenetic product syn- to postdating quartz precipitation and feldspar dissolution, while postdating dolomite precipitation. As it was only observed in one sample, and no paragenetic relation to illite meshworks or pore-bridging illite was observed, it may have formed prior to illite meshworks or pore-bridging illite. Ramseyer (1987) presented both early diagenetic and burial diagenetic anhydrite and barite precipitation phases in the Buntsandstein. Early diagenetic sulfate precipitation was assigned to the formation of a caliche, while the burial diagenetic sulfate precipitation mostly filled intragranular pores while it could not be related to a specific process (Ramseyer, 1987). Kunkel et al. (2018) also observed anhydrite cements encasing quartz overgrowth cements but relate their formation to early diagenetic, possibly hypersaline solutions in a sabkha/playa environment. In this study, its paragenetic relation points to a burial diagenetic origin, likely associated to the burial diagenetic sulfate precipitation (mostly of barite) previously derived by Dubois et al. (1996)) in veins, showing homogenization temperatures of fluid inclusions in barite of 114.4–128.8 °C. Further burial diagenetic barite precipitation in veins and the host rock was also derived by other researchers in the Buntsandstein in the area surrounding the URG (Busch et al., 2024; Böcker, 2020; Bossennec et al., 2021; Soyk, 2015; Griffiths et al., 2016). As vein barite is also associated to sulfide ore mineralizations (Busch et al., 2022), a genetic relation to the Zn-Pb-Ag MVT deposits, e.g., in Wiesloch at the western margin of the URG, dated to the Miocene (Pfaff et al., 2010) is conceivable.

Due to basin inversion from the Cretaceous to Eocene, the studied deposits have been uplifted (Schumacher, 2002). However, as previously described uplift diagenetic (i.e. contact to undersaturated meteoric water close to the surface, sensu Worden et al. (2018) alteration (goethite authigenesis, carbonate nodule dissolution and formation of Wadflecken (Busch et al., 2022; Hübl, 1942)) was not observed, it is likely that the overlying Upper Buntsandstein Röt claystones, Muschelkalk limestones and evaporites, as well as Lower Keuper claystones overlying the Buntsandstein in the studied area (Geyer and Gwinner, 2011) act as sufficient seals against alteration by meteoric waters near the present-day surface. Therefore, uplift diagenetic alteration is not being considered.

5.2. *Reservoir quality controls*

The derived reservoir quality controls in the presented Lower Buntsandstein section generally match well with previously derived controls from other study areas in and around the URG in SW Germany and NE

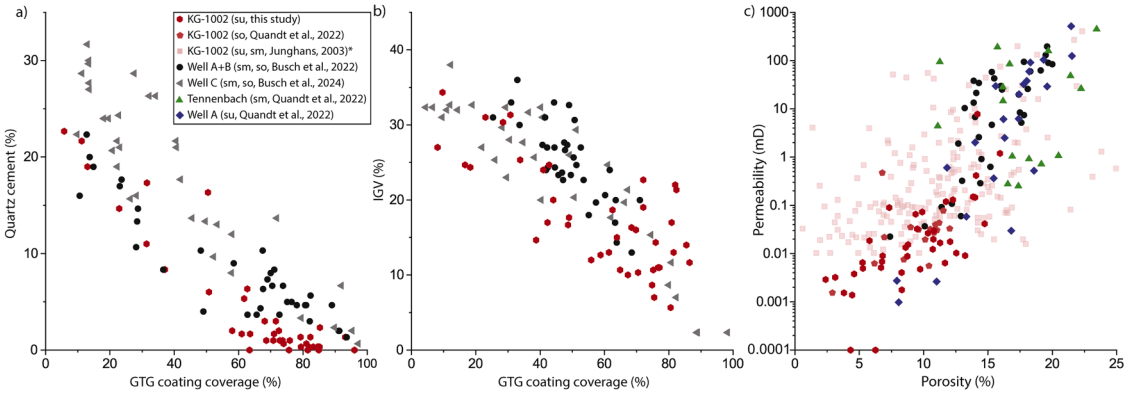

Fig. 17. a) Comparison of GTI coating coverages and quartz cement contents. b) Comparison of the effect of GTG coating coverage on the IGV for available datasets. c) Comparison of published porosity and permeability data for the Lower (su), Middle (sm), and Upper Buntsandstein (so) from the marginal facies of the URG. *The permeability measurements of Junghans (2003) are performed at 0.8 MPa confining stress, whereas all other measurements were performed at 1.2 MPa confining stress. Apparently, the lower measurement limit is also at 0.01 mD, therefore no values below that are plotted. Consequently, derived permeability data are slightly higher than from the other studies.

France (Busch et al., 2022; Busch et al., 2024; Quandt et al., 2022; Schmidt et al., 2020; Busch et al., 2022). While the overall reservoir quality is low, positive permeability anomalies are still related to larger grain sizes when comparing samples of the same porosity range (Fig. 13f), which initially result in larger pore throat sizes, enhancing fluid flow (see also Quandt et al., 2022). This general assessment is in line with previous analyses from Buntsandstein samples specifically (Kunkel et al., 2018) and sand(stone) samples in general (Beard and Weyl, 1973).

Furthermore, the framework stabilizing effect of blocky cements, counteracting compaction, and preserving intergranular volume and thereby porosity and permeability, was also previously derived for other Buntsandstein (e.g., quartz, dolomite, K-feldspar cements in Busch et al., 2022) and Late Triassic sandstones (dolomite cements in Regnet et al., 2024) (Fig. 13c, h, i). However, as especially the quartz cement content is a function of the thermal exposure (Lander et al., 1997; Walderhaug et al., 2000; Lander and Bonnell, 2008), the burial history has to be considered for reservoir quality assessments (Busch et al., 2018). Opposed to samples from the western graben shoulder (Palatine Forest and northern Vosges), and shallowly buried samples in the western part of the Upper Rhine Graben, which show lower maximum quartz cement contents (Busch et al., 2022), samples from the eastern graben shoulder show higher maximum quartz cement contents (Soyk, 2015). This correlation can also be extended to the studied Kraichgau-1002 well on the eastern graben shoulder. More deeply buried samples experiencing higher thermal exposures in the eastern part of the URG, show even higher maximum quartz cement contents, which further reduce the porosity and decrease the reservoir quality (Busch et al., 2024).

While most cited studies in the Buntsandstein highlight a generally porosity-preserving effect of blocky cements (quartz, carbonates, K-feldspar, sulfates), it does not necessarily mean that the preserved permeabilities are economical. While studies from the western part of the central URG show permeabilities up to 200 mD in shallowly buried samples (up to 1500 m present-day depth (Busch et al., 2022)), the reported samples from the eastern graben shoulder, with maximum permeabilities of 7.8 mD have to be critically assessed for a geothermal use case.

As the quartz cement content can be related to the grain coating coverage by illite, they have to be considered as well. GTI coating coverages in core samples from the Buntsandstein in the URG and the graben shoulders have consistently been highlighted to negatively correlate with quartz cement contents (Fig. 17a). The same can be observed in the studied samples (Fig. 11a). However, the effect of porosity preservation by quartz cement inhibition is overprinted by the enhanced chemical compaction at GTG interfaces coated by illite. This enhancement of chemical compaction by illite is often observed in illite coated sandstone lithologies (Heald, 1955; Bjørkum, 1996; Thomson, 1959; Robin, 1978; Molenaar, 1986; Tada and Siever, 1989; Dewers and Ortoleva, 1991). This leads to a counteracting effect on reservoir quality, by enhancing compactional porosity loss in samples containing high GTG coating coverages, while higher GTI coating coverages inhibit syntaxial quartz cementation and may preserve porosity. Furthermore, the radial texture of illite at GTI interfaces, and the observed pore bridging textures have a deteriorating effect on permeability in individual samples (Fig. 13k) (Neasham, 1977). Tangential illite at GTG interfaces reduces porosity and permeability by enhancing chemical compaction, whereas radial illite at GTI interfaces results in a preservation of porosity, by inhibiting syntaxial quartz overgrowth cementation, but also reduces permeability by narrowing the hydraulic diameter at pore throats.

While the effect of enhanced chemical compaction at illite coated GTG contacts has previously been demonstrated for samples from the subsurface of the Upper Rhine Graben, experiencing burial prior to and following Cretaceous inversion, the studied samples show similarly low minimum IGV values and an overall similar correlation between the GTG coating coverage and the IGV (Fig. 17b). Considering that the studied well is located at the eastern graben shoulder and the lithologies did not experience another phase of burial since the Eocene formation of the Upper Rhine Graben, as the two other sample series used for correlation (Busch et al., 2024), this implies that the effect of chemical compaction has already reduced porosity during the initial Mesozoic burial phase.

Ductile rock fragment contents show a poor correlation to reservoir quality and only deteriorate porosity and permeability of individual samples (Fig. 13e). This poor correlation of ductile grains with the IGV and reservoir quality is in contrast to other reservoir scenarios (e.g., Worden et al., 1997; Greve et al., 2024) however, just implies that GTG coatings are more strongly affecting compactional porosity loss in the Buntsandstein of the marginal facies.

As the permeability of only individual samples is positively affected by intragranular dissolution porosity in K-feldspar, chert, and undifferentiated RF (Fig. 13j) a general positive influence on reservoir properties of the Buntsandstein can be excluded. This is also supported by general assessments of intragranular porosity formation, where resulting isolated intragranular pores unlikely contribute to enhanced permeability (Kumar et al., 2023; Pittman, 1979).

Comparison to other published porosity and permeability data from core material from the Buntsandstein in and around the Upper Rhine Graben, highlights that the studied Lower Buntsandstein samples are at the lower end of the porosity permeability range (Fig. 17c). The overall measurement range is overlapping with results of Quandt et al. (2022), who sampled the Upper Buntsandstein from the same well. The measurement data from (Junghans (2003) from the Lower and Middle Buntsandstein (the majority is derived from the Middle Buntsandstein), mostly show comparable porosities, with higher maximum porosities up to 25 %. However, permeabilities are mostly higher at given porosities. It has to be noted, that the measurements by Junghans (2003) were performed at confining pressures of 0.8 MPa, as opposed to measurements of all other compared studies, which were performed at 1.2 MPa confining pressure. The lower confining stresses may be a reason for the higher permeabilities. Stratigraphically comparable samples from the Lower Buntsandstein from well A in Quandt et al. (2022) show markedly higher permeabilities and porosities (Fig. 17c), which implies that the stratigraphic position does not systematically correlate to reservoir properties. Similarly, samples from the Middle Buntsandstein of Junghans (2003), Quandt et al. (2022), and Busch et al. (2022a) cover the whole range of porosities and permeability between 0.01 to 1000 mD.

While the samples from the studied well, located on the graben shoulder, did not experience deep burial since the Eocene (Fig. 2c), as comparable samples from the graben center, but show moderate to poor reservoir qualities, when compared to other core samples (Fig. 17c) they must have experienced the bulk of their burial diagenetic alteration and reservoir quality deterioration prior to the Cretaceous basin inversion.

5.2.1. *Relation of grain coating characteristics and permeability to grain size*

As the Lower Buntsandstein succession in the marginal basin facies in SW-Germany is characterized by a coarsening upward sequence toward the Middle Buntsandstein succession (Leiber and Bock, 2014) and previous studies highlight a generally positive influence of the detrital grain size on reservoir properties in the Buntsandstein (Busch et al., 2024; Quandt et al., 2022; Schmidt et al., 2020; Busch et al., 2022b; Bofill et al., 2025) the relationships of detrital grain size and reservoir quality controls were further evaluated. Although the present study contains some coarse sand-sized samples (Fig. 15c), reservoir quality is lower than in other, finer grained Buntsandstein samples. For available Buntsandstein core samples the correlation between grain size and permeability is poor and overprinted by diagenetic processes, such as cementation and compaction (Fig. 13). This implies that coarse grain size (by itself) is not a suitable criterion to accurately target high reservoir quality sections.

As tangential illite coatings are discussed to be emplaced during clay

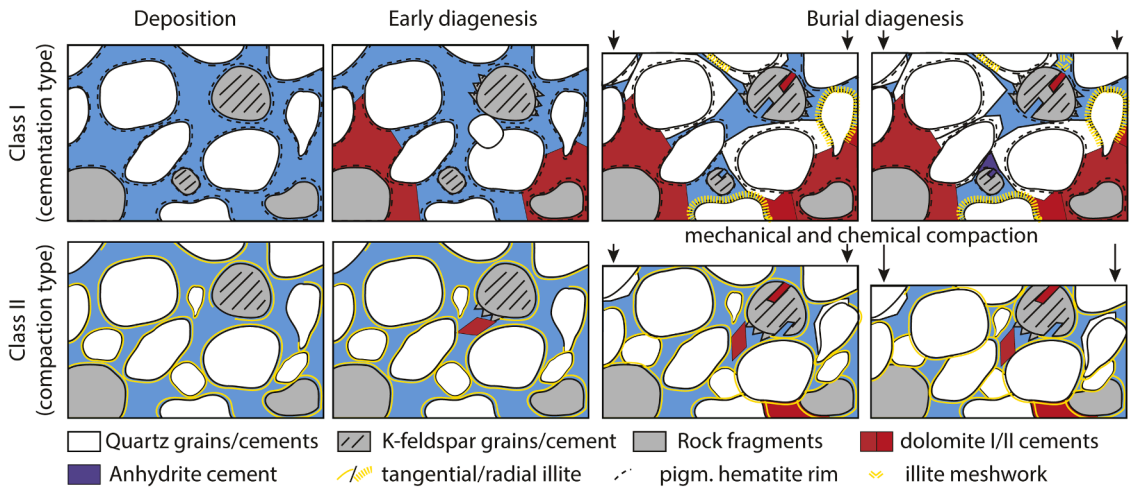

Fig. 18. Schematic reservoir quality development in cementation dominated porosity loss (class I) samples and compaction dominated porosity loss (class II) samples.

mineral illuviation (e.g., Ajdukiewicz et al., 2010) prior to the onset of substantial mechanical compaction, a correlation to detrital grain sizes could be expected and is reported in literature (Aro et al., 2023; Shammari et al., 2011; Wooldridge et al., 2017). The poor correlations between grain size and grain coating coverages (GTI (R^2<0.01) and GTG (R^2=0.19), Fig. 15a, b) implies that detrital grain size and relevant properties affecting reservoir quality (e.g., framework stabilizing cementation at non-grain coated GTI interfaces, enhanced pressure dissolution at illite coated GTG interfaces) in the marginal facies of the Buntsandstein are either unrelated or overprinted by post-depositional processes. While tangential illite grain coatings are contributing to both, GTI and GTG coating coverages, radial illite coatings only contribute to GTI coating coverages, and are a diagenetic product (Clauer et al., 2008). However, the presence of tangential illite is often attributed to promote the later precipitation of radial illite (Gaupp et al., 1993). In the studied samples radial illite is also present on grain surfaces devoid of a tangential clay mineral coating (Fig. 8i, 9e), implying their formation is unaffected by a detrital/early diagenetic precursor clay mineral grain coating. It is therefore unlikely that radial illite coatings are correlated to detrital grain sizes and likely additionally skew the correlation between the grain size and GTI coating coverages.

The non-correlation of grain coating characteristics and detrital grain sizes may furthermore be related to remobilization and tangential grain coating abrasion in semi-arid depositional systems (e.g., Ajdukiewicz et al., 2010; Esch et al., 2008; Busch, 2020), temporally and spatially variable clay mineral infiltration/soil formation (e.g., Ortlam, 1974; Molenaar et al., 2019), or varying clay mineral availability from the sediment source area (Busch, 2020) resulting in the observed tangential grain coating clay mineral distributions. The formation, emplacement, and preservation of grain coating clay minerals in (semi-) arid continental red beds therefore cannot be related to a single granulometric property. However, understanding the spatial variability of grain coating coverages will be key in understanding and predicting reservoir quality differences in the Buntsandstein, given their influence on framework stabilizing blocky cement formation and compactional porosity loss.

Reservoir quality in the Buntsandstein in the area of the URG is a complex interplay of spatially variable enhanced compaction and cementation, closely related to illite grain coatings at GTG and GTI interfaces (Figs. 9a, b, 11b, 13b, d). Where grain coating clay minerals at GTI interfaces are absent, blocky cements can preserve the IGV and higher permeability than in compacted samples with the same porosity (Figs. 13c, g, h, I, 18). In individual samples containing radial illitic GTI coatings, which inhibit syntaxial quartz cement precipitation, thereby preserving porosity (Figs. 8i and 9e), permeability is locally reduced further (Fig. 13k and 18). Anhydrite only reduced inter- and intragranular porosity in a single sample (Fig. 18).

6. Conclusion

The overall poor reservoir quality of Triassic Lower Buntsandstein samples in the studied well section is related to the enhanced compactional porosity loss in samples containing tangential illite as GTG coatings. Samples containing low tangential and radial grain coating coverages (GTI <50 %) are characterized by pervasive quartz overgrowth cements, reducing porosity, but preserving higher permeability than chemically compacted samples in the same porosity range.

While the detrital grain size positively correlates with permeability in the studied samples, the correlation across available core samples from SW-Germany is poor. Furthermore, grain coating characteristics (GTI and GTG coating coverage, which affect reservoir properties) and detrital grain size do only show a poor correlation across available core samples from the Buntsandstein from the URG and adjacent areas. Therefore, just targeting coarse grained sections of the Buntsandstein, will unlikely automatically result in good reservoir quality. This highlights the necessity to integrate reservoir quality controls, rather than using individual proxies based on individual well sections.

CRediT authorship contribution statement

Benjamin Busch: Writing – original draft, Visualization, Methodology, Investigation, Formal analysis, Conceptualization. **Lennart L. Böke:** Writing – review & editing, Investigation, Formal analysis. **Christina Schmidt:** Writing – review & editing, Resources. **Matthias Warnecke:** Writing – review & editing, Resources. **Christoph Hilgers:** Writing – review & editing, Conceptualization.

Declaration of competing interest

The authors declare that they have no known competing financial interests or personal relationships that could have appeared to influence the work reported in this paper.

Acknowledgements

BB and LLB thankfully acknowledge thin section preparation by M. von Dollen at KIT. BB, LLB, and CH thankfully acknowledge permission to publish the results of this study. We thankfully acknowledge core

sampling permission by LGRB, Freiburg. The authors also thankfully acknowledge the constructive review comments by anonymous reviewers and editorial handling by Dr. Zarrouk.

Supplementary materials

Supplementary material associated with this article can be found, in the online version, at doi:10.1016/j.geothermics.2025.103453.

Data availability

All relevant data is made available in supplementary materials.

References

Aehnelt, M., Hilse, U., Pudlo, D., Heide, K., Gaupp, R., 2021. On the origin of bleaching phenomena in red bed sediments of Triassic Buntsandstein deposits in Central Germany. Geochemistry, 125736. https://doi.org/10.1016/j.chemer.2020.125736.

Aigner, T., Bachmann, G.H., 1992. Sequence-stratigraphic framework of the German Triassic. Sediment. Geol. 80, 115–135.

Ajdukiewicz, J.M., Nicholson, P.H., Esch, W.L., 2010. Prediction of deep reservoir quality using early diagenetic process models in the Jurassic Norphlet Formation, Gulf of Mexico. Am. Assoc. Pet. Geol. Bull. 94, 1189–1227. https://doi.org/10.1306/04211009152.

Amthor, J.E., Okkerman, J., 1998. Influence of early diagenesis on reservoir quality of Rotliegende sandstones, Northern Netherlands. Am. Assoc. Pet. Geol. Bull. 82 (12), 2246–2265. https://doi.org/10.1306/00AA7F04-1730-11D7-8645000102C1865D.

Aro, O.E., Jones, S.J., Meadows, N.S., Gluyas, J., Charlaftis, D., 2023. The importance of facies, grain size and clay content in controlling fluvial reservoir quality – an example from the Triassic Skagerrak Formation, Central North Sea, UK. Petroleum Geosci. 29 (2). https://doi.org/10.1144/petgeo2022-043.

Bachmann, G.H., Geluk, M.C., Warrington, G., Becker-Roman, A., Beutler, G., Hagdorn, H., Hounslow, M.W., Nitsch, E., Röhling, H.G., Simon, T., Szulc, A., 2010. Triassic. In: Doornenbal, J.C., Stevenson, A.G. (Eds.), Petroleum Geological Atlas of the Southern Permian Basin Area. EAGE Publications, B.V., Houten, pp. 149–173.

Backhaus, E., 1974. Limnische und fluviatile sedimentation im südwestdeutschen Buntsandstein. Geologische Rundschau 63 (3), 925–942.

Bauer, A., 1994. Diagenese des Buntsandsteins im Bereich der Rheingraben-Westrandstörung bei Bad Dürkheim. Mitt Pollichia 81, 215–289.

Beard, D.C., Weyl, P.K., 1973. Influence of texture on porosity and permeability of unconsolidated sand. Am. Assoc. Pet. Geol. Bull. 57 (2), 349–369.

Bertrand, L., Jusseaume, J., Géraud, Y., Diraison, M., Damy, P.-C., Navelot, V., Haffen, S., 2018. Structural heritage, reactivation and distribution of fault and fracture network in a rifting context: case study of the western shoulder of the Upper Rhine Graben. J. Struct. Geol. 108, 243–255. https://doi.org/10.1016/j.jsg.2017.09.006.

Bjørkum, P.A., 1996. How important is pressure in causing dissolution of quartz in sandstones? J. Sediment. Res. 66 (1), 147–154.

Bloch, S., Lander, R.H., Bonnell, L.M., 2002. Anomalously high porosity and permeability in deeply buried sandstone reservoirs: origin and predictability. Am. Assoc. Pet. Geol. Bull. 86, 301–328. https://doi.org/10.1306/61EEDABC-173E-11D7-8645000102C1865D.

Böcker, J., 2015. Petroleum System and Thermal History of the Upper Rhine Graben. RWTH Aachen University [PhD thesis].

Böcker, J., 2020. Hydrothermal influences in the Römerberg oil field and their impacts on reservoir diagenesis. DGMK/ÖGEW Frühjahrstagung 2020. Celle, Germany.

Böcker, J., Littke, R., 2015. Thermal maturity and petroleum kitchen areas of Liassic Black Shales (Lower Jurassic) in the central Upper Rhine Graben, Germany. Int. J. Earth Sci. 105 (2), 611–636. https://doi.org/10.1007/s00531-015-1188-9.

Bofill, L., Bozetti, G., Schäfer, G., Ghienne, J.-F., Schuster, M., Heap, M.J., Knobelock, G., Scherer, C., Armenlenti, G., de Souza, E., 2025. Sedimentary control on permeability heterogeneity: the middle Buntsandstein continental sandstones (Lower Triassic, eastern France). Mar. Pet. Geol. 173. https://doi.org/10.1016/j.marpetgeo.2024.107261.

Bofill, L., Bozetti, G., Schäfer, G., Ghienne, J.-F., Schuster, M., Scherer, C., de Souza, E., 2024. Quantitative facies analysis of a fluvio-aeolian system: Lower Triassic Buntsandstein Group, eastern France. Sediment. Geol. 465. https://doi.org/10.1016/j.sedgeo.2024.106634.

Bossennec, C., Géraud, Y., Böcker, J., Klug, B., Mattioni, L., Sizun, J.-P., Sudo, M., Moretti, I., 2021. Evolution of diagenetic conditions and burial history in Buntsandstein Gp. fractured sandstones (Upper Rhine Graben) from in-situ δ18O of quartz and 40Ar/39Ar geochronology of K-feldspar overgrowths. Int. J. Earth Sci. 110, 2779–2802. https://doi.org/10.1007/s00531-021-02080-2.

Bossennec, C., Moretti, I., Geraud, Y., Mattioni, L., Daniel, J.-M., Haffen, S., Bourlange, S., Diraison, M., Malartre, F., 2015. Diagenetic features of Buntsandstein Sandstones of the eastern border of the Upper Rhine Graben and implications in terms of burial history. In: 15E Congrès Français de Sédimentologie. Chambéry, France.

Bourquin, S., Bercovici, A., López-Gómez, J., Diez, J.B., Broutin, J., Ronchi, A., Durand, M., Arché, A., Linol, B., Amour, F., 2011. The permian–Triassic transition and the onset of Mesozoic sedimentation at the northwestern peri-Tethyan domain scale: Palaeogeographic maps and geodynamic implications. Palaeogeogr. Palaeoclimatol. Palaeoecol. 299 (1–2), 265–280. https://doi.org/10.1016/j.palaeo.2010.11.007.

Bourquin, S., Guillocheau, F., Péron, S., 2009. Braided rivers within an arid alluvial plain (example from the Lower Triassic, western German Basin): Recognition criteria and expression of stratigraphic cycles. Sedimentology 56 (7), 2235–2264. https://doi.org/10.1111/j.1365-3091.2009.01078.x.

Bourquin, S., Péron, S., Durand, M., 2006. Lower Triassic sequence stratigraphy of the western part of the Germanic Basin (west of Black Forest): fluvial system evolution through time and space. Sediment. Geol. 186 (3–4), 187–211. https://doi.org/10.1016/j.sedgeo.2005.11.018.

Busch, B., 2020. Pilot study on provenance and depositional controls on clay mineral coatings in active fluvio-eolian systems, western USA. Sediment. Geol. 406, 105721. https://doi.org/10.1016/j.sedgeo.2020.105721.

Busch, B., Adelmann, D., Herrmann, R., Hilgers, C., 2022a. Controls on compactional behavior and reservoir quality in a Triassic Buntsandstein reservoir, Upper Rhine Graben, SW Germany. Marine Petroleum Geol. 136, 105437. https://doi.org/10.1016/j.marpetgeo.2021.105437.

Busch, B., Böcker, J., Hilgers, C., 2024. Improved reservoir quality assessment by evaluating illite grain coatings, quartz cementation, and compaction – case study from the Buntsandstein, Upper Rhine Graben, Germany. Geoenergy Sci. Eng. 241, 213141. https://doi.org/10.1016/j.geoen.2024.213141.

Busch, B., Hilgers, C., Adelmann, D., 2020. Reservoir quality controls on Rotliegend fluvio-aeolian wells in Germany and the Netherlands, Southern Permian Basin – Impact of grain coatings and cements. Mar. Pet. Geol. 112, 104075. https://doi.org/10.1016/j.marpetgeo.2019.104075.

Busch, B., Hilgers, C., Gronen, L., Adelmann, D., 2017. Cementation and structural diagenesis of fluvio-aeolian Rotliegend sandstones, northern England. J. Geol. Soc. London. 174, 855–868. https://doi.org/10.1144/jgs2016-122.

Busch, B., Hilgers, C., Lander, R.H., Bonnell, L.M., Adelmann, D., 2018. Reservoir quality and burial model evaluation by kinetic quartz and illite cementation modeling: case study Rotliegendes, N-Germany. Am. Assoc. Pet. Geol. Bull. 101 (2), 293–307. https://doi.org/10.1306/0503171605217075.

Busch, B., Spitzner, A.-D., Adelmann, D., Hilgers, C., 2022b. The significance of outcrop analog data for reservoir quality assessment: a comparative case study of Lower Triassic Buntsandstein sandstones in the Upper Rhine Graben. Mar. Pet. Geol. 141. https://doi.org/10.1016/j.marpetgeo.2022.105701.

Clauer, N., Liewig, N., Ledesert, B., Zwingmann, H., 2008. Thermal history of triassic sandstones from the Vosges Mountains-Rhine Graben rifting area, NE France, based on K-Ar illite dating. Clay. Miner. 43 (3), 363–379. https://doi.org/10.1180/claymin.2008.043.3.03.

Clauser, C., Villinger, H., 1990. Analysis of conductive and convective heat transfer in a sedimentary basin, demonstrated for the Rheingraben. Geophys. J. Int. 100 (3), 393–414.

Dewers, T., Ortoleva, P., 1991. Influences of clay minerals on sandstone cementation and pressure solution. Geology. 19, 1045–1048.

Dickson, J.A.D., 1965. A modified staining technique for carbonates in thin section. Nature 205, 587.

Dubois, M., Ayt Ougougdal, M., Meere, P., Royer, J.-J., Boiron, M.-C., Cathelineau, M., 1996. Temperature of paleo- to modern self-sealing within a continental rift basin : the fluid inclusion data (Soultz-sous-Forêts, Rhine graben, France). Eur. J. Mineral. 8, 1065–1080.

Duringer, P., Aichholzer, C., Orciani, S., Genter, A., 2019. The complete lithostratigraphic section of the geothermal wells in Rittershoffen (Upper Rhine Graben, eastern France): a key for future geothermal wells. BSGF - Earth Sci. Bull. 190. https://doi.org/10.1051/bsgf/2019012.

Esch, W.L., Ajdukiewicz, J.M., Reynolds, A.C., 2008. Early grain-coat formation in Chaco Dune Field, New Mexico: insight into formation mechanisms, distribution, and implications for predictive modeling to assist in deep play identification. In: AAPG Annual Convention. San Antonio, TX, Tulsa, Oklahoma, USA: AAPG.

Evans, B., Kohlstedt, D.L., 1995. Rheology of rocks, rock physics & phase relations. AGU Reference Shelf 148–165.

Folk, R.L., 1980. Petrology of Sedimentary Rocks. Hemphill Publishing Company, Austin, Texas, U.S.A., p. 182

Folk, R.L., Ward, W., 1957. Brazos River bar: a study in the significance of grain-size parameters. J. Sediment. Petrol. 27, 3–26. https://doi.org/10.1306/74D70646-2B21-11D7-8648000102C1865D.

Füchtbauer, H., 1967. Der Einfluss des Ablagerungsmilieus auf die Sandsteindiagenese im Mittleren Buntsandstein. Sediment. Geol. 1, 159–179.

Füchtbauer, H., 1998. Sedimente Und Sedimentgesteine, p. 1141. Schweizerbart, Stuttgart.

Gaupp, R., Matter, A., Platt, J.D., Ramseyer, K., Walzebuck, J., 1993. Diagenesis and fluid evolution of deeply buried Permian (Rotliegend) gas reservoirs, northwest Germany. Am. Assoc. Pet. Geol. Bull. 77 (7), 1111–1128. https://doi.org/10.1306/BDFF8E0C-1718-11D7-8645000102C1865D.

Gaupp, R., Okkerman, J.A., 2011. Diagenesis and reservoir quality of Rotliegend sandstones in the northern Netherlands - a review. In: Grötsch, J., Gaupp, R. (Eds.), The Permian Rotliegend of the Netherlands, 98. Society for Sedimentary Geology, pp. 193–226.

Geyer, O.F., Gwinner, M.P., 2011. Geologie von Baden-Württemberg, Stuttgart, Germany. E. Schweizerbart'sche Verlagsbuchhandlung (Nägele u. Obermiller) 627.

Greene, G.W., Kristiansen, K., Meyer, E.E., Boles, J.R., Israelachvili, J.N., 2009. Role of electrochemical reactions in pressure solution. Geochim. Cosmochim. Acta 73, 2862–2874. https://doi.org/10.1016/j.gca.2009.02.012.

Greve, J., Busch, B., Quandt, D., Knaak, M., Hilgers, C., 2024a. Understanding the interplay of depositional rock types, mineralogy, and diagenesis on reservoir properties of the coal-bearing Langsettian and Duckmantian strata (Bashkirian,

Pennsylvanian) of the Ruhr Area, NW Germany. Int. J. Earth Sci. https://doi.org/10.1007/s00531-024-02454-2.
Greve, J., Busch, B., Quandt, D., Knaak, M., Hilgers, C., 2024b. The influence of sedimentary facies, mineralogy, and diagenesis on reservoir properties of the coal-bearing Upper Carboniferous of NW Germany. Petroleum Geosci. 30 (1). https://doi.org/10.1144/petgeo2023-020.
Griffiths, L., Heap, M.J., Wang, F., Daval, D., Gilg, H.A., Baud, P., Schmittbuhl, J., Genter, A., 2016. Geothermal implications for fracture-filling hydrothermal precipitation. Geothermics. 64, 235–245. https://doi.org/10.1016/j.geothermics.2016.06.006.
Haffen, S., Géraud, Y., Diraison, M., Dezayes, C., 2013. Fluid-flow zones in a geothermal sandstone reservoir: localization from thermal conductivity and temperature logs, borehole EPS1 (Soultz-sous-Forêts,France) and 3D models. In: Thirty-Eighth Workshop on Geothermal Reservoir Engineering. Stanford University, Stanford, California.
Heald, M.T., 1955. Stylolites in sandstone. J. Geol. 63, 101–114. https://doi.org/10.1086/626237.
Heald, M.T., Larese, R.E., 1974. Influence of coatings on quartz cementation. J. Sediment. Petrol. 44 (4), 1269–1274. 10.1306/212F6C94-2B24-11D7-8648000102C1865D.
Houseknecht, D.W., 1987. Assessing the relative importance of compaction processes and cementation to reduction of porosity in sandstones. Am. Assoc. Pet. Geol. Bull. 71, 633–642.
Hübl, H.H., 1942. Der gebleichte Mittlere Buntsandstein („Rehbergschichten“ b^{2b}) von Bergzabern-Westmark. Beiträge zur naturkundlichen Forschung im Oberrheingebiet 7, 301–358.
Junghans, W.-D., 2003. Fazies, Zyklizität, Petrophysik und Paläomagnetik im Buntsandstein der Bohrung Kraichgau 1002 (SW-Deutschland)Frisch, W, Kuhlemann, J (Eds.), In: Tübinger Geowissenschaftliche Arbeiten. Tübingen, Germany, p. 191.
Kristiansen, K., Valtiner, M., Greene, G.W., Boles, J.R., Israelachvili, J.N., 2011. Pressure solution - the importance of the electrochemical surface potential. Geochim. Cosmochim. Acta 75, 6882–6892. https://doi.org/10.1016/j.gca.2011.09.019.
Kumar, A., Prajapati, N., Späth, M., Busch, B., Schneider, D., Hilgers, C., Nestler, B., 2023. Qualitative dissolution modeling of etch-pit formation on the K-feldspar surface through phase-field approach. J. Geophys. Res.: Solid Earth 128 (4). https://doi.org/10.1029/2022jb025749.
Kunkel, C., Aehnelt, M., Pudlo, D., Kukowski, N., Totsche, K.U., Gaupp, R., 2018. Subsurface aquifer heterogeneities of lower triassic clastic sediments in central Germany. Mar. Pet. Geol. 97, 209–222. https://doi.org/10.1016/j.marpetgeo.2018.06.022.
Lander, R.H., Bonnell, L.M., 2008. Toward more accurate quartz cement models: the importance of euhedral versus noneuhedral growth rates. Am. Assoc. Pet. Geol. Bull. 92 (11), 1537–1563.
Lander, R.H., Larese, R.E., Bonnell, L.M., 2008. Toward more accurate quartz cement models: the importance of euhedral versus noneuhedral growth rates. Am. Assoc. Pet. Geol. Bull. 92 (11), 1537–1563. https://doi.org/10.1306/07160808037.
Lander, R.H., Walderhaug, O., Bonnell, L.M., 1997. Application of sandstone diagenetic modeling to reservoir quality prediction and basin history assessment. In: Memorias del I Congreso Latinoamericano de Sedimentología. Caracas, Venezuela: Sociedad Venezolana de Geólogos.
Lanson, B., Beaufort, D., Berger, G., Bauer, A., Cassagnabère, A., Meunier, A., 2002. Authigenic kaolin and illitic minerals during burial diagenesis of sandstones: a review. Clay. Miner. 37 (1), 1–22. https://doi.org/10.1180/0009855023710014.
Leggewie, R., Füchtbauer, H., El-Najjar, R., 1977. Zur Bilanz des Buntsandsteinbeckens (Korngrößenverteilung und Gesteinsbruchstücke). Geologische Rundschau 66 (1), 551–577.
Leiber, J., Bock, H., 2014. Der Buntsandstein in der Kraichgau-Senke und der südwestdeutschen Randfazies (Baden-Württemberg). Schriftenreihe der Deutschen Gesellschaft für Geowissenschaften 69, 525–546. https://doi.org/10.1127/sdgg/69/2014/525.
Lippmann, R., 2012. Diagenesis in Rotliegend, Triassic and Jurassic clastic Hydrocarbon Reservoirs of the Central Graben, North Sea. Friedrich-Schiller-University, Jena [PhD thesis].
Lundegard, P., 1992. Sandstone porosity loss - A “big picture” view of the importance of compaction. J. Sediment. Petrol. 62 (2), 250–260. 10.1306/D42678D4-2B26-11D7-8648000102C1865D.
Mader, D., 1982. Genese des mitteleuropäischen Buntsandsteins. Naturwissenschaften. 69 (7), 311–325.
Miall, A.D., 1978. Lithofacies types and vertical profile models in braided river deposits: a summary. In: Miall, A.D. (Ed.), Fluvial sedimentology, Can Soc Petrol Geol Mem, 5, 1 ed. Geological Survey of Canada, Calgary, Alberta, Canada, pp. 597–604.
Molenaar, N., 1986. The interrelation between clay infiltration, quartz cementation, and compaction in lower Givetian terrestrial sandstones, northern Ardennes, Belgium. J. Sediment. Res. 56 (3), 359–369. 10.1306/212F8913-2B24-11D7-8648000102C1865D.
Molenaar, N., Felder, M., 2018. Clay cutans and the origin of illite rim cement: an example from the siliciclastic Rotliegend Sandstone in the Dutch Southern Permian Basin. J. Sediment. Res. 88 (5), 641–658. https://doi.org/10.2110/jsr.2018.33.
Molenaar, N., Vaznytė, J., Šliaupa, S., 2019. Aridisols in the Southern Permian Basin, key to understand clay cement distribution. Int. J. Earth Sci. 108 (7), 2391–2406. https://doi.org/10.1007/s00531-019-01769-9.
Monsees, A.C., Busch, B., Hilgers, C., 2021. Compaction control on diagenesis and reservoir quality development in red bed sandstones: a case study of Permian Rotliegend sandstones. Int. J. Earth Sci. 110 (5), 1683–1711. https://doi.org/10.1007/s00531-021-02036-6.
Monsees, A.C., Busch, B., Schöner, N., Hilgers, C., 2020. Rock typing of diagenetically induced heterogeneities – A case study from a deeply-buried clastic Rotliegend reservoir of the Northern German Basin. Mar. Pet. Geol. 113, 104163. https://doi.org/10.1016/j.marpetgeo.2019.104163.
Morad, S., Aldahan, A.A., 1987. Diagenetic “replacement” of feldspars by titanium oxides in sandstones. Sediment. Geol. 51 (3–4), 147–153. https://doi.org/10.1016/0037-0738(87)90045-5.
Neasham, J.W., 1977. The morphology of dispersed clay in sandstone reservoirs and its effect on sandstone shaliness, pore space and fluid flow properties. In: SPE Annual Fall Technical Conference and Exhibition. Denver, CO.
Nitsch, E., 2024. Buntsandstein in Baden-Württemberg. LGRB-Informationen, Freiburg im Breisgau.
Oelkers, E.H., Bjørkum, P., Murphy, W.M., 1996. A petrographic and computational investigation of quartz cementation and porosity reduction in North Sea sandstones. Am. J. Sci. 296 (4), 420–452.
Ölmez, J.A., Busch, B., Hilgers, C., 2024. Reservoir quality of upper cretaceous limestones (Ahlen-Fm., Beckum Member, Münsterland Cretaceous Basin): effects of cementation and compaction on the compactable depositional volume. Int. J. Earth Sci. https://doi.org/10.1007/s00531-024-02411-z.
Ortlam, D., 1974. Inhalt und Bedeutung fossiler Bodenkomplexe in Perm und Trias von Mitteleuropa. Geol. Rundsch. 63, 850–884.
Paxton, S.T., Szabo, J.O., Ajdukiewicz, J.M., Klimentidis, R.E., 2002. Construction of an intergranular volume compaction curve for evaluating and predicting compaction and porosity loss in rigid-grain sandstone reservoirs. Am. Assoc. Pet. Geol. Bull. 86 (12), 2047–2067. https://doi.org/10.1306/61EEDDFA-173E-11D7-8645000102C1865D.
Pfaff, K., Hildebrandt, L.H., Leach, D.L., Jacob, D.E., Markl, G., 2010. Formation of the Wiesloch Mississippi Valley-type Zn-Pb-Ag deposit in the extensional setting of the Upper Rhinegraben, SW Germany. Miner. Depos. 45 (7), 647–666. https://doi.org/10.1007/s00126-010-0296-5.
Pittman, E.D., 1979. Porosity, diagenesis and productive capability of sandstone reservoirs. In: Scholle, P.A., Schluger, P.R. (Eds.), Aspects of Diagenesis. SEPM Society for Sedimentary Geology, pp. 159–174.
Quandt, D., Busch, B., Schmidt, C., Hilgers, C., 2022. Diagenesis and controls on reservoir quality of lower triassic red bed sandstones (Buntsandstein) from a marginal basin facies, Southwest Germany. Marine Petroleum Geol. 142, 105744. https://doi.org/10.1016/j.marpetgeo.2022.105744.
Ramseyer, K., 1987. Diagenese des Buntsandsteins und ihre Bbeziehung zur tektonischen Entwicklung der Nordschweiz. Eclogae Geol. Helv. 80, 383–395. https://doi.org/10.5169/seals-166002.
Regnet, J.B., Bailly, C., Bourquin, S., Robion, P., Poujol, M., Sengelen, X., Serrano, O., Ledésert, B., 2024. Paleosol-induced early dolomitization with U Pb age constraints and its implications for fluid pathways in ancient sandstone aquifers. Sediment. Geol. 470, 106719. https://doi.org/10.1016/j.sedgeo.2024.106719.
Reinhardt, L., Ricken, W., 2000. The stratigraphic and geochemical record of Playa Cycles: monitoring a Pangaean monsoon-like system (Triassic, Middle Keuper, S. Germany). Palaeogeogr. Palaeoclimatol. Palaeoecol. 161 (1–2), 205–227. https://doi.org/10.1016/S0031-0182(00)00124-3.
Rimstidt, J.D., Barnes, H.L., 1980. The kinetics of silica-water reactions. Geochim. Cosmochim. Acta 62, 1851–1863. https://doi.org/10.1016/0016-7037(80)90220-3.
Robin, P.-Y.F., 1978. Pressure solution at grain-to-grain contacts. Geochim. Cosmochim. Acta 42 (9), 1383–1389. https://doi.org/10.1016/0016-7037(78)90043-1.
Röhling, H.G., Lepper, J., 2013. Paläogeographie des mitteleuropäischen Beckens während der tieferen Trias (Buntsandstein). Schriftenreihe der Deutschen Gesellschaft für Geowissenschaften 69, 43–67. https://doi.org/10.1127/sdgg/69/2014/43.
Rupf, I., Nitsch, E., 2008. Das geologische Landesmodell von Baden-Württemberg: Datengrundlagen, technische Umsetzung und erste geologische Ergebnisse: Regierungspräsidium Freiburg, Abteilung 9. Landesamt für Geologie. Rohstoffe und Bergbau (LGRB).
Schmidt, C., 2022. Compaction and Cementation Controls on Reservoir Quality in Buntsandstein Red Beds. KIT, Karlsruhe Germany [PhD Thesis].
Schmidt, C., Busch, B., Hilgers, C., 2020a. Lateral variations of detrital, authigenic and petrophysical properties in an outcrop analog of the fluvial Plattensandstein, Lower Triassic, Central Germany. Zeitschrift der Deutschen Geologischen Gesellschaft 172 (4), 541–564. https://doi.org/10.1127/zdgg/2020/0234.
Schmidt, C., Busch, B., Hilgers, C., 2020b. Compaction and cementation control on bleaching in triassic fluvial red beds, S-Germany. Zeitschrift der Deutschen Gesellschaft für Geowissenschaften 174 (4), 523–539. https://doi.org/10.1127/zdgg/2020/0233.
Schumacher, M.E., 2002. Upper Rhine Graben: role of preexisting structures during rift evolution. Tectonics. 21 (1). https://doi.org/10.1029/2001tc900022, 6-1-6-17.
Shammari, S., Franks, S., Soliman, O., 2011. In: Depositional and Facies Controls on Infiltrated/Inherited Clay Coatings: Unayzah Sandstones, Saudi Arabia. AAPG Annual Convention and Exhibition. AAPG, Houston, Texas, USA, Tulsa, Oklahoma, USA.
Slunitschek, K., Kolb, J., Eiche, E., 2021. Lithium extraction from geothermal brines: Modern adsorption method for raw material extraction. Wiley Analytical Science Magazine.
Soyk, D., 2015. Diagenesis and Reservoir Quality of the Lower and Middle Buntsandstein (Lower Triassic), SW Germany. Ruprecht-Karls-University, Heidelberg [PhD thesis].
Stephenson, L.P., Plumley, W.J., Placiauskas, V.V., 1992. A model for sandstone compaction by grain interpenetration. J. Sediment. Res. 62 (1), 11–22. https://doi.org/10.1306/D4267875-2B26-11D7-8648000102C1865D.
Tada, R., Siever, R., 1989. Pressure solution during diagenesis. Annu Rev. Earth. Planet. Sci. 17 (1), 89–118. https://doi.org/10.1146/annurev.ea.17.050189.000513.

Thomson, A., 1959Ireland, H.A. (Ed.), Silica in Sediments, 7. SEPM Society for Sedimentary Geology, pp. 92–111.
Underhill, J.R., de Jonge-Anderson, I., Hollinsworth, A.D., Fyfe, L.C., 2023. Use of exploration methods to repurpose and extend the life of a super basin as a carbon storage hub for the energy transition. Am. Assoc. Pet. Geol. Bull. 107 (8), 1419–1474. https://doi.org/10.1306/04042322097.
Walderhaug, O., Lander, R.H., Bjørkum, P.A., Oelkers, H., Bjørlykke, K., Nadeau, P.H., 2000. Modelling quartz cementation and porosity in reservoir sandstones: examples from the Norwegian continental shelf. In: Worden, R.H., Morad, S. (Eds.), Quartz Cementation in Sandstones, 29. Blackwell Science Ltd., Oxford, pp. 39–49.
Walker, T.R., 1967. Formation of red beds in modern and ancient deserts. GSA Bull. 78, 353–368.
Wilson, M.D., Stanton, P.T., 1994. Diagenetic mechanisms of porosity and permeability reduction and enhancement. Wilson MD, Reservoir Quality Assessment and Prediction in Clastic Rocks SEPM Short Course 30 (SEPM), 59–119.
Wooldridge, L.J., Worden, R.H., Griffiths, J., Utley, J.E.P., 2017. Clay-coated sand grains in petroleum reservoirs: understanding their distribution via a modern analogue. J. Sediment. Res. 87 (4), 338–352. https://doi.org/10.2110/jsr.2017.20.
Worden, R.H., Armitage, P.J., Butcher, A.R., Churchill, J.M., Csoma, A.E., Hollis, C., Lander, R.H., Omma, J.E., et al., 2018. Petroleum reservoir quality prediction: overview and contrasting approaches from sandstone and carbonate communities. In: Armitage, P.J., Butcher, A.R., Churchill, J.M., Csoma, A.E., Hollis, C., Lander, R. H., et al. (Eds.), Reservoir Quality of Clastic and Carbonate Rocks: Analysis, Modelling and Prediction, Special Publications, 435. Geological Society, London, pp. 1–31.
Worden, R.H., Mayall, M.J., Evans, I.J., 1997. Predicting reservoir quality during exploration: lithic grains, porosity and permeability in tertiary clastic rocks of the South China Sea basin. Geol. Soc. London, Special Publications 126 (1), 107–115. https://doi.org/10.1144/gsl.Sp.1997.126.01.08.
Ziegler, P., 1990. Geological Atlas of Western and Central Europe, 2nd edition. Shell Internationale Petroleum Maatschappij BV, Geological Society of London, Elsevier, Amsterdam: Shell Internationale Petroleum Maatschappij BV, p. 232.
Ziegler, P.A., 1982. Triassic rifts and facies patterns in Western and Central Europe. Geologische Rundschau 71 (3), 747–772. https://doi.org/10.1007/bf01821101.